PRDM16 functions as a co-repressor in the BMP pathway to suppress neural stem cell proliferation

Li He[1], Jiayu Wen[2, *] and Qi Dai[1, *]

1 Department of Molecular Bioscience, the Wenner-Gren Institute, Stockholm University

2 Division of Genome Sciences and Cancer, The John Curtin School of Medical Research, The Australian National University and Australian Research Council Centre of Excellence for the Mathematical Analysis of Cellular Systems.

* Co-corresponding authors

Abstract

BMP signalling acts as an instructive cue in various developmental processes such as tissue patterning, stem cell proliferation, and differentiation. However, it is not fully understood how this signalling pathway generates different cell-specific outputs. Here we have identified PRDM16 as a key co-factor for BMP signalling. PRDM16 contributes to a repressive role of BMP signalling on neural stem cell (NSC) proliferation. We demonstrate that PRDM16 regulates the genomic distribution of BMP pathway transcription factors, the SMAD4/pSMAD complex, preventing the activation of cell proliferation genes. When *Prdm16* is lost, the SMAD complex relocates to nearby genomic regions, leading to abnormal upregulation of BMP target genes. This function of PRDM16 is also required for the specification of choroid plexus (ChP) epithelial cells. Through a single-cell resolution fluorescent *in situ* approach, we have observed that genes co-repressed by SMAD and PRDM16, such as *Wnt7b* and several cell cycle regulators, become overexpressed in *Prdm16* mutant ChP. Our findings elucidate a mechanism through which SMAD4 and pSMAD1/5/8 repress gene expression. Moreover, our study suggests a regulatory circuit composed of BMP and Wnt signaling, along with PRDM16, in controlling stem cell behaviors.

Introduction

Uncontrollable cell proliferation can lead to tumor growth, while premature differentiation can result in tissue degeneration. The balance between stem cell proliferation and differentiation is a crucial aspect in developmental and stem cell biology. BMP (Bone morphogenetic proteins) signaling is a key cell-signaling pathway in regulating stem cell proliferation and maintaining adult stem cell quiescence [1-3]. Moreover, BMP signaling is essential in various cell specification processes [4-6].

The ability of a single pathway to play a diverse range of roles relies on context-specific transcriptional outputs. BMPs signal through two types of SMAD proteins: the receptor SMADs (R-SMADs) - Smad1, 5 and 8, and the co-SMAD protein SMAD4. Upon ligand binding, heterodimeric receptors like BMPRI and BMPRII phosphorylate R-SMADs, leading to the assembly and nuclear translocation of the SMAD complex with SMAD4. This complex then regulates gene expression by binding to enhancers of BMP target genes. Apart from transducing BMP signaling, SMAD4 is an essential effector in TGF-β/Activin signaling. In response to ligands such as TGF-β and Activin, SMAD4 associates with two other R-SMADs - phosphorylated SMAD 2 and 3, regulating downstream genes of the TGF-β/Activin signaling pathway. These SMADs recognize and directly bind to two main types of short DNA motifs in target enhancers via their N-terminal MH1 domain [7]. However, since the binding is generally weak, SMAD complexes rely on various co-factors such as transcription factors, co-activators and co-repressors to activate or repress target gene expression [8].

In the mammalian brain, BMP and Wnt signaling pattern the brain midline where an essential structure, the ChP, emerges. Neural epithelial cells at the presumptive ChP site lose neural potential and exit cell cycle. Only a small number of cells at the boarder of the ChP primordium and cortical hem (CH) persist as slowly dividing ChP progenitors, leading to the expansion of the monolayered ChP epithelial cells [9]. BMP signaling is essential for ChP epithelium specification. Conditional depletion of the BMP receptor *BMPr1a* diminishes ChP development [10], whereas ectopic BMP transforms neural progenitors into ChP cells [11]. Wnt signaling, peaking at CH, is also necessary for ChP epithelial cell specification [12]. Conditional depletion of ß-Catenin results in defective ChP, and overexpression of ß-Catenin expands CH at the expense of the ChP epithelium. These findings emphasize the importance of tightly controlling Wnt and BMP signaling levels for proper cell specification.

The PR domain-containing (PRDM) family protein PRDM16 determines cell fate specification in various cell types [13-19]. Previous studies, including our own, demonstrated that *Prdm16* knockout (KO) mouse brains show severely reduced ChP structures [20-22]. Interestingly, it was shown that PRDM16 can interact with TGF-ß pathway SMAD proteins *in vitro* and impact TGF-ß signaling output in craniofacial tissues [21,23]. PRDM16 is also a downstream effector of BMP signaling during brown adipocyte specification [24,25]. A recent study reported that PRDM16 and its ortholog PRDM3 (also known as Evi1) regulate Wnt signaling during craniofacial development in zebrafish [26]. These findings suggest that PRDM16 may be more broadly involved in regulating BMP/TGF-ß and Wnt signaling. However, the underlying molecular mechanisms remain unclear.

Consistent with its essential roles in normal development, mutations and dysregulation of *Prdm16* are linked with several human diseases, including those identified in the patients with 1p36 chromosomal aberrations and cardiomyopathy [27]. PRDM16 exhibits versatile functions at the molecular level, regulating chromatin accessibility and epigenetic states of its bound enhancers [18,20]. Depending on associated cofactors, PRDM16 can either repress or activate gene expression. This dual role poses a challenge when considering PRDM16 as a therapeutic target, as undesired outcome may occur. Thus, a comprehensive understanding of the regulatory roles of this protein in each specific process is crucial for effective disease treatment strategies.

In this study we have investigated the mechanisms that regulate the transition between stem cell proliferation and differentiation during ChP development. We show that *Prdm16* mutant ChP cells fail to exit cell cycle, a similar phenotype to when BMP signaling is abolished [10]. Using primary NSC culture, we dissected the molecular interaction of SMAD4/pSMAD1/5/8 proteins with PRDM16, and found that PRDM16 functions as a co-repressor that holds the SMAD complex at distal enhancers, repressing genes involved in cell proliferation. Finally, we validated that some of the co-regulated genes by BMP signaling and PRDM16 become de-repressed in the *Prdm16* mutant ChP. These findings uncover an essential function of PRDM16 in stem cell regulation and BMP and Wnt signalling.

Results

PRDM16 promotes cell cycle exiting of neural epithelial cells at the ChP primordium

To understand how *Prdm16* regulates ChP epithelial specification, we first investigated the expression of this gene in the developing mouse brain. At embryonic day 10.5 (E10.5), BMP signaling specifies the presumptive ChP [10]. *Prdm16* mRNAs and nuclear localization of the PRDM16 protein become detectable in the presumptive ChP at this stage (**Fig. 1A, supplementary Fig. 1A**). As previously shown, *Prdm16*^{cGT}, a *Prdm16* knockout allele (*Prdm16 KO*), displayed severely reduced ChP structure at E13.5 (**Fig 1B)** [20-22]. Expression of *Ttr*, a classic ChP marker gene, is reduced in both the lateral ventricle (tChPs) (**Fig. 1C**) and the fourth ventricle (hChP) (**Supplementary Fig. 1B**) in the *Prdm16 KO* mutant, suggesting that the function of PRDM16 is not area-restricted but generally required for ChP development.

To assess the patterning of the CH and ChP regions, we analyzed the expression of *Wnt2b* and *BMP4* using conventional RNA *in situ* hybridization. *Wnt2b* expression, which marks the CH, appeared comparable between *Prdm16* KO and control brains at E11.5 and E12.5 (**Supplementary Fig. 1C**), indicating that CH development is not affected by the loss of *Prdm16*. BMP4, which labels the ChP and CH, also showed normal expression levels and spatial distribution in the mutant brain. These findings suggest that the BMP-dependent patterning of the ChP and CH domain remains intact in the absence of *Prdm16*.

However, the ChP epithelial layer in *Prdm16* mutants remained abnormally thick, resembling the adjacent neural epithelium (**Fig. 1C, Supplementary Fig. 1C**). This observation led us to investigate the underlying cellular changes responsible for the ChP defects in the mutant. To assess cell proliferation, we performed a 2-hour EdU labeling at E12.5. In control embryos, ChP cells were largely EdU negative and formed a monolayer, indicating that most had exited the cell cycle. In contrast, *Prdm16* mutant ChP cells marked by *β-Gal* remained highly proliferative (**Fig. 1D**). These results suggest several possibilities: ChP epithelial cells is not properly specified in the mutant, mutant ChP cells are specified but fail to exit the cell cycle to differentiate, or both processes are impaired.

To explore these possibilities, we first examined the cell type composition of *Prdm16* mutant ChP cells at E12.5. We stained brain sections from control and mutant embryos with the neuronal marker Doublecortin (Dcx). In controls, Dcx-positive cells were absent from the ChP,

139 indicating that neural epithelial cells had successfully transitioned into ChP epithelial cells and
140 lost their neural potential (**Fig. 1E**). In contrast, the *Prdm16* mutant ChP exhibited numerous
141 Dcx-positive cells along the basal side of the epithelium, suggesting ongoing neurogenesis.

142 We next examined the expression of the NSC marker SOX2. In control brains, SOX2 is highly
143 expressed in NSCs adjacent to the ChP epithelium but is significantly downregulated within
144 the presumptive ChP region (**Supplementary Fig. 1D**). This downregulation was absent in the
145 *Prdm16* mutant. Together, these results indicate that at E12.5, *Prdm16* depletion disrupts the
146 normal transition of neural progenitors into ChP epithelial cells, maintaining cells in a
147 proliferative, undifferentiated state.

148 We then asked whether PRDM16 not only regulates ChP epithelial specification but also
149 directly restricts cell proliferation. To test this, we examined *Prdm16* mutant ChP cells at a later
150 stage. We performed double S-phase labeling by injecting EdU at E12.5 and BrdU at E13.5,
151 followed by sample collection at E14.5. By this stage, the wild-type ChP had developed into an
152 elongated, monolayered epithelium in which most cells were negative for both EdU and BrdU,
153 indicating cell cycle exit. In contrast, the *Prdm16* mutant ChP remained a disorganized cluster
154 of cells, many of which were EdU-positive, BrdU-positive, or both (**Fig. 1F-G**). This finding
155 suggests that although the mutant ChP can separate from the neuroepithelium at later stages, it
156 fails to exit the cell cycle and differentiate, supporting a direct role of PRDM16 in restricting
157 proliferation.

158 Given that BMP signaling is a key regulator of ChP formation and that the BMP pathway
159 mutants such as *Foxg1-cre*::loxp*Bmpr1a* also exhibit ectopic cell proliferation in the
160 developing ChP [10], we next investigated whether PRDM16 interacts with the BMP pathway to
161 control cell proliferation.

162 **PRDM16 and BMP signaling collaborate to induce NSC quiescence *in vitro***

163 To investigate the molecular interplay between PRDM16 and BMP signaling in regulating cell
164 proliferation, we turned to primary NSCs as an *in vitro* model. BMP signaling is known to
165 maintain quiescence in adult NSC *in vivo* and can induce proliferative NSCs into quiescence *in*
166 *vitro* [1]. Furthermore, previous studies have shown that embryonic cortical NSCs are responsive
167 to BMP4 treatment [28], making them a suitable system for probing downstream BMP signaling

168 events. Based on this, we established a cell culture assay to evaluate the effects of BMP4 and
169 PRDM16 on NSC proliferation and quiescence (**Fig. 2A**).

170 Unexpectedly, we found that PRDM16 protein levels were undetectable in cultured NSCs
171 despite high levels of *Prdm16* mRNAs (**Supplementary Fig. 2A-B**). Given that the PRDM16
172 protein is normally restricted to the nucleus of NSCs in embryonic brain tissues (**Fig. 1B**,
173 **Supplementary Fig.1A** and [20]), this observation suggests that *in vivo* mechanisms may regulate
174 PRDM16 protein stability and nuclear localization. Post-translational modification of PRDM16
175 has been identified as a key regulatory mechanism in brown adipocytes [29], and we speculate a
176 similar mechanism may operate in NSCs.

177 To bypass this limitation and examine PRDM16's molecular function in regulating NSC
178 proliferation and gene regulation, we generated a lenti-viral construct expressing
179 *3xNSL_Flag_Prdm16* under a constitutive promoter. Infection of wild-type primary NSCs with
180 this construct yielded a cell line with robust *Prdm16* mRNA expression and detectable nuclear
181 PRDM16 protein (**Supplementary Fig. 2A-B**), which we referred to as
182 *Prdm16_overexpressing (Prdm16_OE)*. For comparison, we attempted to establish three
183 additional lines: wild-type NSCs infected with the empty vector (*wt_CDH*), *Prdm16_KO* NSCs
184 infected with the empty vector (KO_CDH), and *Prdm16_KO* NSCs infected with
185 *3xNSL_Flag_Prdm16.* However, we were unable to generate the last line despite repeated
186 attempts. This failure was likely due to low viral production (the *Prdm16* coding sequence
187 exceeds 3kb) and the increased sensitivity of KO NSCs to viral infection. Nevertheless, we
188 proceeded with comparative analyses of *Prdm16_OE* cells against *wt_CDH*, *KO_CDH* and
189 uninfected *KO* NSCs.

190 To assess cell proliferation rates, we labeled NSCs with EdU and mKi67. BMP4 treatment of
191 *Prdm16_OE* NSCs led to a marked reduction in the number of mKi67- and EdU-positive
192 populations (**Fig. 2B-D**). Following BMP4 washout, *Prdm16_OE* NSCs restored EdU and
193 mKi67 labeling, indicating re-entry into the cell cycle. This reversible reduction confirms that
194 BMP4 induces a quiescent, non-proliferative state in NSCs. In contrast, a larger proportion of
195 *Prdm16*_KO cells failed to exit the cell cycle in response to BMP4, as shown by a less
196 pronounced decrease in mKi67- and EdU-positive populations (**Fig. 2B-D**). Notably,
197 *Prdm16_KO* cells exhibited similar properties regardless of whether they were infected with
198 the control viral vector (**Supplementary Fig. 2D-F)**, and we therefore used both lines
199 interchangeably in our analyses.

200 Previous studies have shown that BMP4 can program ChP cell fate and activate ChP-specific
201 genes in neural progenitors cultured *in vitro* [11]. To test whether PRDM16 cooperates with BMP
202 signaling to induce ChP gene expression, we measured *Ttr* mRNA levels using reverse-
203 transcription followed by quantitative PCR (RT-qPCR). In *Prdm16_OE* NSCs, *Ttr* expression
204 was robustly induced following BMP4 treatment. In contrast, *Prdm16*_KO NSCs and NSCs
205 lacking the *Prdm16*_OE construct failed to upregulate *Ttr* in response to BMP4 (**Fig. 2E,**
206 **Supplementary Fig. 2G**).

207 Together, these results indicate that both BMP signaling and PRDM16 are required not only to
208 restrict NSC proliferation but also to induce ChP gene expression. We next investigated the
209 molecular mechanisms underlying this cooperation.

210 **BMP signaling and PRDM16 cooperatively repress proliferation genes.**

211 To understand how BMP signaling and PRDM16 suppress cell proliferation, we aimed to
212 determine the transcriptional targets of SMAD4 and pSMAD1/5/8 in cells with and without
213 BMP4. We first applied Cleavage Under Targets and Tagmentation (CUT&TAG) experiments
214 using a PRDM16 antibody and the available SMAD antibodies to profile their genomic binding
215 sites. The PRDM16 antibody worked efficiently, but none of the SMAD antibodies produced
216 libraries with sufficient sequencing reads. Subsequently we employed chromatin
217 immunoprecipitation followed by deep-sequencing (ChIP-seq) for the SMAD proteins. Given
218 that SMAD4 forms a complex with SMAD2/3 only in response to TGF-β/activin-type ligands,
219 we included an antibody targeting SMAD3 as a control for non-BMP4-induced SMAD4
220 binding. Thus, our experiment settings enabled us to profile genomic binding sites for PRDM16,
221 SMAD4 and two types of R_SMADs under conditions with endogenous BMPs and TGF-
222 β/Activin, as well as ectopic BMP4.

223 In *Prdm16_OE* cells without BMP4, we identified several hundred to a few thousand ChIP-seq
224 peaks for all three classes of SMAD proteins after normalizing to the input reads (FDR < 10%),
225 indicating endogenous levels of BMP and TGF-β signaling in these cells (**Fig. 3A,**
226 **Supplementary Fig. 3A-C**). Following BMP4 addition, pSMAD1/5/8 exhibited approximately
227 a 750-fold increase in peak number, while the number of SMAD3 peaks increased by less than
228 threefold (**Fig. 3A**, **Supplementary Fig. 3A**). Furthermore, in cells treated with BMP4, the
229 pSMAD1/5/8 peaks largely overlap with the SMAD4 peaks, but much less with the SMAD3
230 peaks (**Supplementary Fig. 3B**). For example, pSMAD1/5/8 binds to two enhancers in the

231 intronic region of *Prdm16,* with the binding intensity dramatically increased in response to
232 BMP4 (**Supplementary Fig. 3D**). This suggests that *Prdm16* itself is a transcriptional target of
233 BMP signaling. Indeed, *Prdm16* mRNA levels were elevated by BMP4 in wild-type but not
234 *Prdm16_KO* cells (**Supplementary Fig. 2B**). By contrast, SMAD3 showed little ChIP-seq
235 signal in the *Prdm16* gene locus even in the presence of BMP4. These results confirm that the
236 response of pSMAD1/5/8 is specific to BMP4, while SMAD3 is generally unresponsive to
237 BMP4. The gained Smad3 sites likely result from an indirect effect of BMP signaling.

238 To evaluate the regulatory activity of SMAD4/pSMAD1/5/8 in NSCs, we determined the state
239 of transcription activation using H3K4me3 CUT&TAG signals at annotated gene transcription
240 start sites (TSS) in BMP4-treated and untreated *Prdm16_OE* cells. As cell identity genes are
241 known to be marked by extended breadth of H3K4me3 [30], we reasoned that compared to RNA-
242 seq, which measures all gene products, changes in the H3K4me3 signal at the promoter might
243 bias toward cell identity genes between proliferation and quiescence states. Thus, we
244 determined all BMP4-repressed and activated genes by measuring changes in the H3K4me3
245 CUT&TAG read coverage at annotated TSS in BMP4-treated *Prdm16_OE* cells compared to
246 untreated, identifying 282 up-regulated and 429 down-regulated genes (**Fig. 3B**) ($P<0.01$). To
247 pinpoint genes directly regulated by SMAD4 and pSMAD1/5/8, we intersected the
248 dysregulated genes with those whose regulatory regions contain overlapping SMAD4 and
249 pSMAD1/5/8 ChIP-seq peaks. This analysis led to the identification of 145 up-regulated and
250 184 down-regulated SMAD4 and pSMAD1/5/8 target genes.

251 To elucidate the function of BMP-regulated targets, we performed gene ontology (GO) analyses
252 for the genes that changed expression in response to BMP4 in *Prdm16_OE* cells and were also
253 bound by SMAD4 and pSMAD1/5/8. Remarkably, the downregulated genes (BMP4-repressed
254 genes), but not the up-regulated genes (BMP4-activated genes), showed significantly enriched
255 functional categories, with nearly all GO terms related to cell proliferation/cell cycle (**Fig. 3C**).
256 A recent study reported that BMP2-induced genes are enriched for neuronal and astrocyte
257 differentiation [31], while our analysis did not identify these categories. One possibility for the
258 discrepancy is that we overexpress *Prdm16* in cultured NSCs, which may reinforce BMP
259 signaling activities in cell proliferation. Other possibilities could be the use of different BMP
260 ligands (BMP4 versus BMP2), differences in the origin of NSC culture (ours was from E13
261 instead of E11 and E14), or different profiling methods (H3K4me3 versus RNA-seq).

262 To identify PRDM16-repressed and activated genes under active BMP signaling conditions,
263 we compared changes of H3K4me3 coverage at TSSs between BMP4-treated *Prdm16_KO*
264 cells and BMP4-treated *Prdm16_OE* cells. We found approximately twice as many up-
265 regulated genes (240) as down-regulated genes (132) (**Fig. 3D**), suggesting that the cooperative
266 activity of PRDM16 and BMP signaling mainly represses gene expression. We further
267 overlapped the 184 genes repressed by BMP4 and the 240 genes repressed by PRDM16,
268 identifying 31 common ones. These 31 genes displayed low H3K4me3 coverage in
269 *Prdm16_OE* cells with BMP4 but higher H3K4me3 signal in both *Prdm16_KO* cells treated
270 with BMP4 and untreated *Prdm16_OE* cells **(Fig. 3E).**

271 Next, we attempted to validate whether changes in TSS H3K4me3 intensity correspond to
272 changes in mRNA levels, by conducting RT-qPCR for selected genes whose function is
273 associated with cell proliferation from the gene ontology analysis: *Wnt7b*, *Mybl2*, *Id3*, *Spc24*
274 and the three *Spc24*-related genes (*Spc25*, *Ndc80* and *Nuf2*) (**Fig. 3F-G, Supplementary Fig.**
275 **3E-K**). SPC24 forms the NDC80 kinetochore complex along with three other proteins: SPC25,
276 NDC80 and NUF2 [32] (Illustrated in **Supplementary Fig. 3H**), and their function is essential
277 for chromosome segregation and spindle checkpoint activity. Notably, *Spc25*, *Ndc80* and *Nuf2*
278 appeared repressed by PRDM16 and BMP4 based on changes in H3K4me3 at the TSS
279 (**Supplementary Fig. 3E**), despite not being identified as the top 31 candidates. mRNA levels
280 for most of the tested genes followed a similar pattern to the H3K4me3 intensity: BMP4-treated
281 *Prdm16_OE* cells showed the lowest expression, while either the loss of *Prdm16* or absence of
282 BMP4 led to upregulation. *Spc24* gene products showed minimal amplification in qPCR, likely
283 due to poor primer sequence quality or unstable mRNAs. Another exception is *Id3* whose
284 expression increased upon BMP4 treatment or *Prdm16* depletion, indicating PRDM16
285 repressing *Id3* but BMP4 inducing *Id3*. However, the activation of *Id3* by BMP4 is significantly
286 stronger in *Prdm16_KO* cells than that in *Prdm16_OE* cells, suggesting that BMP signaling
287 normally activates *Id3* but PRDM16 suppresses such activation. In contrast, *Cdkn1a,* a target
288 gene of TGF-β pathway encoding the cell cycle inhibitor P21*,* exhibited consistent H3K4me3
289 coverage and mRNA levels across BMP4 treated and non-treated cells, as well as between
290 *Prdm16_OE* and *KO* cells (**Fig. 3F-G**), confirming that neither PRDM16 nor BMP signaling
291 influences *Cdkn1a* expression in NSCs.

292 **PRDM16 assists genomic binding of SMAD4 and pSMAD1/5/8**

293 To understand how PRDM16 interacts with BMP signaling, we integrated PRDM16
294 CUT&TAG data with SMAD ChIP-seq data, focusing on assessing PRDM16's influence on
295 the genomic binding of SMAD proteins.

296 The SEACR peak caller software [33] identified 3337 and 7639 PRDM16 CUT&TAG common
297 peaks from four replicates of BMP4-treated and untreated *Prdm16_OE* samples (FDR < 10%,
298 see Methods), respectively (**Fig. 4A**). Upon BMP4 treatment, there were 5936 lost and 1634
299 gained PRDM16 CUT&TAG peaks, suggesting that PRDM16 regulates a distinct subset of
300 genes in proliferating versus quiescent NSCs. Samples from *Prdm16_KO* cells lacked these
301 sites, confirming the specificity of the PRDM16 CUT&TAG signal (**Fig. 4B**).

302 From our overlapping analyses (see Methods), we found that over 50% of SMAD4 and
303 pSMAD1/5/8 binding peaks were consistent in *Prdm16_OE* and *Prdm16_KO* cells
304 (**Supplementary Fig. 4A-B**), indicating that deletion of *Prdm16* does not affect general
305 genomic binding ability of these proteins. Using Homer's mergePeaks function with PRDM16
306 CUT&TAG and SMAD ChIP-seq data, we identified co-bound sites by PRDM16 and SMAD
307 proteins in BMP4-treated *Prdm16_OE* cells. PRDM16 CUT&TAG peaks mainly overlap with
308 SMAD4 and pSMAD1/5/8 peaks, but not much with SMAD3 peaks (**Supplementary Fig. 4A-**
309 **C**). This result suggests that PRDM16 mainly collaborates with the SMAD4/pSMAD1/5/8
310 complex but not the SMAD3/SMAD4 complex in cells with high levels of BMP4.

311 Further examination of SMAD4 and pSMAD1/5/8 binding revealed significantly lower
312 enrichment of SMAD4 and pSMAD1/5/8 at PRDM16 co-bound sites in *Prdm16_KO* cells
313 compared to *Prdm16_OE* cells (**Fig. 4C**) (P=2.5E-6, and P=4.7E-3, respectively, two-tailed *t*-
314 test). As a control, the SMAD4 and pSMAD1/5/8 sites without PRDM16 co-binding did not
315 show such change (P>0.05). This result suggests that SMAD binding to the PRDM16 co-
316 binding sites depends on PRDM16.

317 To validate the co-binding of SMAD4 and PRDM16, we selected the candidate loci, *Wnt7b* and
318 *Id1* (**Fig. 4D-E**) and applied sequential ChIP-qPCR. This experiment confirmed simultaneous
319 binding of SMAD4 and PRDM16 to the same DNA molecules at these loci (**Supplementary**
320 **Fig. 4D**), as SMAD4 was more enriched in the chromatin pulled by the PRDM16 antibody
321 compared to the IgG control. Additionally, ChIP-qPCR confirmed reduced SMAD binding at
322 the SMAD/PRDM16 co-bound site in *Prdm16_KO* cells compared to *Prdm16_OE* cells (**Fig.**

323 **4F-G**). Thus, PRDM16 enhances genomic binding of the SMAD proteins to specific genome
324 regions.

325 **PRDM16 facilitates SMAD4 binding to regions enriched for SMAD palindromic motifs**

326 We then wondered whether there is sequence feature that distinguishes the regions co-bound
327 by SMADs and PRDM16 from those only bound by SMADs. To this end, we checked SMAD-
328 bound regions with PRDM16 binding and those without for two types of SMAD4 binding
329 motifs [8]. Together with pSMAD1/5/8 or pSMAD3, SMAD4 may bind to a palindromic motif,
330 GTCTAGAC or direct repeats of GTCT like GTCTGTCTGTCT [34-36]; together with
331 pSMAD1/5/8, SMAD4 associates with GC-rich SBEs (SMAD-binding elements) including
332 GGCGCC-AN4-GNCV and GRCGNCNNNNNGTCT [37-39]. We calculated occurrence
333 frequency of each of these motifs in binned SMAD4 ChIP-seq peaks from *Prdm16_OE* cells
334 treated with BMP4 (bin 1 to 5 with low to high peak scores, **Fig. 4H**). Interestingly, the
335 palindromic motif is the most enriched one. Its occurrence frequency increases with peak scores,
336 but becomes lower in the SMAD4 peaks absent for PRDM16 co-binding. The frequency of the
337 GTCT-triplet motif also increases with higher SMAD4 peak scores, while there is no reduction
338 in regions without PRDM16 binding. The two GC-rich motifs show a distinct trend: they are
339 not as highly enriched, their frequencies do not increase with higher SMAD4 peak scores, and
340 the occurrence frequency in PRDM16 co-bound regions is either comparable to or even lower
341 than the regions without PRDM16 binding. Together, this result suggests that PRDM16 may
342 separate the SMAD4/pSMAD1/5/8 proteins into two types of genomic regions, one enriched
343 for the palindromic motif where PRDM16 is present and the other with the GC-rich motifs.

344 **SMAD4 and pSMAD1/5/8 switch genomic locations in the absence of PRDM16**

345 Our careful inspection on the *Wnt7b* and *Id1* loci surprisingly revealed that there are multiple
346 ectopic SMAD4 and pSMAD1/5/8 peaks in the *Prdm16* mutant sample (arrow-indicated peaks
347 in **Fig. 5A-B**). We then globally assessed the extent of ectopic SMAD binding surrounding the
348 SMAD/PRDM16 co-bound sites by quantifying differential SMAD binding intensity between
349 *Prdm16_KO* and *Prdm16_OE* cells (**Fig. 5C,** FDR < 10%). In agreement with the metaplots
350 (**Fig. 4C**), all of the SMAD/PRDM16 co-bound sites (blue dots) showed reduced ChIP-seq read
351 coverage in *Prdm16_KO* cells. By contrast, the flanking regions within the 200kb range of a
352 co-bound site (red dots) displayed a trend of increase of SMAD binding in *Prdm16_KO* cells.
353 This result agrees with the aforementioned motif analysis that PRDM16 helps to localize the

354 SMAD complex at specific genomic regions, and it also suggests that without *Prdm16*, the
355 SMAD factors are partly redirected to neighboring genomic regions.

356 **AP1 is the potential co-factor that interacts with relocated SMAD proteins**

357 We intended to find out how SMAD4 and pSMAD1/5/8 relocate to ectopic sites in the absence
358 of *Prdm16*. By running *de novo* motif discovery (see Methods), we identified a number of
359 significantly enriched DNA motifs from pSMAD1/5/8 and SMAD4 ChIP-seq peaks in
360 *Prdm16_OE* and *Prdm16_KO* cells (**Fig. 5D-E**). Interestingly, in addition to the known SMAD
361 motifs, the only other motif identified in both pSMAD1/5/8 and SMAD4 peaks from
362 *Prdm16_KO* cells but not *Prdm16_OE* cells is the AP1 motif. Furthermore, the AP1 motif is
363 more frequently found in the pSMAD1/5/8 and SMAD4 regions lacking PRDM16 binding than
364 those with PRDM16 binding (**Supplementary Fig. 4E**). The interaction between the AP-1
365 complex with the SMAD proteins was reported previously [40]. Our result implies that AP-1 is a
366 potential cofactor for the SMAD proteins in the absence of *Prdm16*. To validate this finding,
367 we performed ChIP-qPCR with an antibody against c-FOS, one of the subunits of AP1, on
368 *Prdm16_OE* and *KO* cells. Supporting the global analyses, c-FOS is enriched in the Smad4-
369 bound regions at the *Wnt7b* and *Id3* loci in the *Prdm16_KO* condition (**Fig. 5F-G**). There is
370 little c-FOS binding to these regions in cells expressing *Prdm16*, suggesting that there is
371 cooperativity of SMAD and AP-1 which facilitates each other's binding when PRDM16 is
372 absent. Alternatively, PRDM16 may suppress genomic accessibility of these regions for SMAD
373 and AP-1 proteins, a function we reported for PRDM16 in cortical NSCs [20].

374 Together, our genomic data and validation suggest an enhancer switch model (**Fig. 5H)**:
375 PRDM16 assists SMAD protein binding to repressive cis-regulatory elements that are enriched
376 for GTCTAGAC palindromic motifs; loss of PRDM16 results in genomic relocation of SMAD
377 proteins, presumably via the association with coactivators such as AP1; the consequence of
378 SMAD relocation is de-repression of cell proliferation regulators.

379 **SMADs and PRDM16 co-repressed genes in NSCs are suppressed in the developing ChP**

380 Next, we investigated whether genes co-regulated by PRDM16 and BMP signaling in NSCs
381 (**Fig. 3C**) are also involved in ChP development, where both factors limit NSC proliferation ([10]
382 and **Fig. 1**). Using published E12.5 mouse brain single cell RNA-seq (scRNA-seq) data [41], we
383 analyzed expression of the 31 co-repressed genes across ChP epithelial (*Ttr*+), CH (BMP4+/

384 *Ttr*-) and a few forebrain-specific radial glia (RG) (Sox2+/Hes5+) clusters (**Fig. 6A,**
385 **Supplementary Fig. 5A**). Except for one gene *Mrtfb* that was not found in the scRNA-seq data,
386 thirteen showed no or weak expression (**Supplementary Fig. 5A**), and seventeen had moderate
387 to high expression in at least one cluster (**Fig. 6A**). Notably, these genes were generally
388 expressed at lower levels in ChP clusters than in CH or RG clusters, suggesting repression in
389 the ChP.

390 To test for direct PRDM16 regulation, we performed CUT&TAG assays using the PRDM16
391 antibody on dissected dorsal midline tissues that mainly contain CH and the ChP (**Fig 6B** and
392 **Supplementary Fig. 5B**) and identified 3238 common peaks across three replicates. Manual
393 inspection of the 31 loci revealed PRDM16 binding near the TSS of 25 genes using the browser
394 Embryonic Mouse Brain Epigenome Atlas [42] (Text in black in **Fig. 6A** and **Supplementary**
395 **Fig. 5A**). Using an unbiased peak-to-promoter mapping, 24/31 co-repressed and 84/153 BMP-
396 only-repressed genes had PRDM16 binding in E12.5 ChP. The enrichment in the co-repressed
397 group (**Supplementary Fig. 5C,** Fisher's Exact Test, p = 0.015) indicates a stronger regulatory
398 role of PRDM16 on these genes in the developing ChP.

399 As an example, *Wnt7b* has two PRDM16 peaks (**Fig 6C**), one unique to the dorsal midline
400 tissue. Given Wnt signaling's role in ChP specification and NSC proliferation[12,43]. *Wnt7b* likely
401 represents a direct PRDM16 target in the developing ChP.

402 **PRDM16 represses *Wnt7b* and Wnt activity in the developing ChP**

403 We sought to determine which of the identified genes from NSC culture are regulated by
404 PRDM16 in the developing ChP. In addition to *Wnt7b*, several other Wnt ligands are expressed
405 in the CH and ChP region [44]. For example, *Wnt3a* is expressed in the dorsal-midline region but
406 not in the forebrain, which explains why it was not identified from the forebrain-derived NSC
407 datasets. Although there is no PRDM16 CUT&TAG peak within the *Wnt3a* locus in cultured
408 NSCs, a PRDM16 CUT&TAG peak is present in the intronic region of *Wnt3a* in the dorsal
409 midline tissue (**Supplementary Fig.5D**). We thus examined the scRNA-seq data [41] and
410 confirmed that multiple components in the Wnt and BMP pathways are present in the CH and
411 ChP clusters (**Supplementary Fig.5E**). To systematically measure expression changes of
412 PRDM16 target genes in the *Prdm16* mutant brain, we applied a multiplexed fluorescent *in situ*
413 approach, Single-Cell Resolution in Situ Hybridization On Tissues (SCRINSHOT) [45]. In this
414 method each mRNA molecule is hybridized with three gene-specific padlock probes and

visualized by florescent dye-conjugated detection probes. A dot of fluorescent signal corresponds to one mRNA molecule, allowing quantitative measurement of gene expression in single cell resolution.

We designed probes for ten Wnt and five BMP pathway components, other genes that are co-repressed by BMP and PRDM16 in NSC culture, as well as cell-type specific markers (the ChP marker gene *Ttr* and *Foxj1*, the neural progenitor markers *Sox2*, *Hes5* and *Zbtb20,* and the neuronal marker Ngn2), and conducted SCRINSHOT in three pairs of control and *Prdm16* mutant brains.

In the control brain, the *Ttr* and Foxj1 probes detect the ChP epithelium but not the adjacent tissues at E11.5 and E12.5, confirming the signal specificity of SCRINSHOT. Several Wnt (*Wnt2b*, *Wnt7b*, *Wnt5a*, *Wnt3a*, *Fzd10* and *Axin2*) and BMP components (*BMP4* and *BMP7*) also display tissue specificity: the Wnt genes are more enriched at CH while the BMP genes are more at the ChP. The representative images from E11.5 and E12.5 samples are presented in **Fig. 7A-B**. Except *Wnt2b*, the other tested *Wnt* genes exhibit low expression in the ChP cells, consistent with the notion that Wnt signaling is present and required at the ChP [12].

Next, we quantified expression changes of these genes in *Prdm16* mutant CH and ChP cells. As expression of *Wnt2b* was relatively unchanged in the mutant (**Supplementary Fig. 1** and **Fig. 7A**), we used *Wnt2b*-expressing cells to define the CH cells and those expressing *Ttr* to define ChP cells in the wild-type brain slice. There were about 110 cells in each region of one brain slice. Because the mutant brain slice showed little *Ttr* signal, we only used the *Wnt2b*-expressing cells to define the anterior border between CH and neocortex and included 110 cells under the border for the CH cells, and the further 110 cells for the mutant ChP cells, as shown in the images with DAPI and cell outlines (**Fig. 7A and Fig. 7D**). We then measured the dot count of each gene in these 220 cells in each sample, and summarized the changes from three pairs of animals in the violin plots (**Fig. 7C** and **Supplementary Fig. 6A**). Expression of *Ttr* and *Foxj1* is severely reduced, while *Sox2*, *Hes5* and *Ngn2* all become upregulated in the mutant ChP, indicating a fate transformation of ChP epithelial to neural cells. This agrees with our immunostaining and conventional *in situ* results (**Fig. 1** and **Supplementary Fig. 1**). Similar to BMP4, other BMP components we tested including *BMP7*, *Smad6*, *Smad7 and Nog* are unchanged, suggesting that PRDM16 is not an upstream regulator of the BMP pathway.

445 Moreover, *Wnt3a* and *Wnt7b* are significantly upregulated in the *Prdm16* mutant ChP (**Fig. 7B-**
446 **E** and **Supplementary Fig. 6A-C**). In line with this, the Wnt target gene *Axin2* is also
447 upregulated, indicating aberrantly elevated Wnt signaling in the *Prdm16* mutant ChP. Thus, the
448 normal function of *Prdm16* represses WNT signaling in the developing ChP.

449 **Levels of Wnt activity correlate with cell proliferation in the developing ChP and CH**

450 We further assessed the relationship between Wnt signaling and cell proliferation in the ChP
451 and CH at E12.5, by correlating expression levels of *mKi67* with *Wnt3a*, *Wnt7b* and *Axin2*
452 levels in wild-type and mutant samples. A significant increase of *mKi67* expression in *Prdm16*
453 mutant ChP cells at E12.5 is accompanied by significantly increased Wnt gene expression (**Fig.**
454 **7F** and **Supplementary Fig 6B-C**). In contrast, little or no increase of *mKi67* signal is found
455 in the mutant CH, suggesting that the effect of PRDM16 is mainly cell-autonomous. We then
456 performed linear regression and Pearson correlation analyses to assess correlations between
457 ChP markers, BMP and Wnt genes. Interestingly, the level of *Axin2* best correlates the level of
458 m*Ki67*, even better than that with other Wnt genes in both wild-type ($r = 0.46$; $p < 2.2$ E-35)
459 and mutant ($r= 0.56$; $p < 1.6$ E-55) CH and ChP cells **(Fig. 7G** and **Supplementary Fig. 6D**).
460 This result suggests that Wnt activity may be responsible for cell proliferation in the CH and
461 ChP region. Supporting this finding, it was shown that ectopic Wnt signaling converts ChP
462 cells into proliferative CH neural cells [12]. Similarly, in the 4th ventricle, two Wnt genes, *Wnt1*
463 and *Wnt3a*, and *mKi67* all became ectopically expressed in *Prdm16* mutant ChP cells
464 (**Supplementary Fig. 7**). Thus, PRDM16 also suppresses Wnt signaling in the hindbrain ChP.

465 Additionally, six cell-proliferation-related genes (Spc24, Spc25, Nuf2, Ndc80, Id3 and Mybl2)
466 exhibited upregulation in *Prdm16* mutant ChP (**Supplementary Fig. 8**). Interestingly, all four
467 NDC80 complex genes became upregulated, pointing to its potential role in promoting NSC
468 proliferation. Taken together, our results suggest that specification of the ChP epithelium
469 requires a process transitioning proliferating NSCs into quiescence, and that this process is
470 mediated by a suppressive role of PRDM16 on Wnt signaling and cell cycle regulators.

471

472

473

474 **Discussion**

475 In this study we reveal a novel molecular mechanism by which BMP signaling regulates cell
476 proliferation and gene expression. We find that PRDM16 acts as a tethering factor to localize
477 the SMAD4/pSMAD1/5/8 complex at specific genomic sites and facilitate the repressive role
478 of the SMAD proteins. The genes co-repressed by PRDM16 and BMP signaling include those
479 encoding Wnt pathway ligands and other cell proliferation regulators.

480 Combinatory activities of morphogens are exploited throughout animal development and tissue
481 homeostasis. The crosstalk between BMP and WNT signaling is complex as it can be
482 synergistic or antagonistic [46]. Surprisingly, both types of effects exist in the specification of
483 ChP epithelium. Here BMP signaling induces NSC quiescence, as evidenced by the presence
484 of ectopic proliferating cells at the ChP in *Bmpr1a* mutant mice [10], while Wnt signaling
485 promotes proliferation since the gain-of-function condition of beta-Catenin phenocopies
486 *Bmpr1a* mutant animals [12]. On the other hand, adding a low dose of Wnt activator to cell culture
487 medium enhances programing efficiency of ChP epithelial cells induced by BMP4 [47], and loss-
488 of-function of beta-Catenin resulted in under-developed ChP structure [12], suggesting that BMP
489 and WNT signaling collaborate to promote ChP epithelial cell differentiation. Our work
490 demonstrated that PRDM16 ensures the right balance of BMP and Wnt activity by maintaining
491 a low level of Wnt gene expression in the developing ChP.

492 PRDM16 was shown to physically interact with SMAD3 [23] and antagonize TGF-β-induced cell
493 cycle arrest [48]. However, we did not detect stable PRDM16/SMAD4/pSMAD1/5/8 or
494 PRDM16/SMAD4/SMAD3 complexes in co-immunoprecipitation assays (data not shown).
495 Instead, sequential ChIP revealed that PRDM16 and SMAD4 bind to the same DNA molecule,
496 supporting their cooperative function at co-occupied regulatory elements. Notably, SMADs
497 when associated with PRDM16 compared to those without PRDM16, with SMADs
498 preferentially bind palindromic motifs in the presence of PRDM16 and GC-rich SBE motifs in
499 its absence, suggesting that PRDM16 modulates SMAD DNA-binding specificity and shifts
500 SMAD regulatory output.

501 A recent study similarly reported that PRDM16 acts as a SMAD4 co-repressor during
502 pancreatic ductal adenocarcinoma progression [49]. There, SMAD4 stably binds the PRDM16
503 promoter and switches its co-factor from the co-repressor PRDM16 (under low TGF-β) to the
504 co-activator SMAD3 (under high TGF-β), depending on TGF-β levels. This mechanism differs

505 from our model. Our data indicate that high BMP4 levels promote SMAD4 and pSMAD1/5/8
506 binding to target loci, including *Prdm16*, resulting in both gene repression and activation.
507 Notably, PRDM16 contributes to the repression function of the SMAD complex even under
508 elevated BMP conditions.

509 Although PRDM16 has been shown to promote proliferation by antagonizing anti-proliferation
510 activity of TGF-β and SMAD3 [48], our data demonstrate that PRDM16 collaborates with
511 SMAD4 and pSMAD1/5/8 to repress proliferation genes, which is consistent with BMP-
512 induced quiescence. Similar roles have been observed in other contexts, such as such as
513 osteoblast differentiation and maturation [50]. Supporting this, genomic profiling revealed that
514 under high BMP4 and PRDM16 conditions, pSMAD1/5/8 and SMAD4 occupy numerous loci
515 without SMAD3, suggesting PRDM16 primarily modulates BMP target genes in these settings.

516 Moreover, while it was reported that PRDM16 enhances Wnt signaling by stabilizing nuclear
517 beta-Catenin in the craniofacial tissue [26], we detected the opposite outcome in the ChP and
518 cultured NSCs, ectopic WNT gene expression in the absence of *Prdm16*, suggesting that
519 PRDM16 represses Wnt genes in these contexts. Notably, PRDM16, Wnt and BMP co-exist in
520 various developmental settings, such as craniofacial development [21,26,51], heart formation [27,52,53],
521 limb patterning [21,54,55], adult intestinal stem cells [56-58] *etc*. We speculate a similar regulatory
522 circuit is used in some, if not all, of these settings.

523 ChP epithelial cells derive from proliferating NSCs, without intermediate fate-commitment
524 steps. This property endows ChP cells with higher plasticity and makes them more vulnerable
525 to abnormal genetic and cellular change, to which high occurrence frequency of ChP tumors in
526 fetuses and young children may be attributed [59]. As an essential brain structure, the ChP releases
527 cerebrospinal fluid (CSF) and acts as a brain-blood barrier [60-62]. Its dysfunction has been linked
528 with several types of human diseases including hydrocephalus, Alzheimer's disease, multiple
529 sclerosis [62]. Deepening our knowledge on the development of ChP will provide new insights
530 into potential therapeutics to prevent or treat ChP tumors and other ChP-related diseases.

531 **Footnote**: a study on the antagonism between PRDM16 and SMAD4 was published on Feb 24,
532 2023 (Hurwitz, 2023) after we posted our manuscript at BioRxiv and during our submission
533 process.

534

535 **Materials and methods**

536 **Animals**

537 All animal procedures were approved by Swedish agriculture board (Jordbruks Verket) with
538 document number Dnr 11553-2017 and 11766-2022. The *Prdm16*^{cGT} mice [22] were maintained
539 by outcrossing with the FVB/NJ line.

540 **In situ hybridization**:

541 To make probes for conventional RNA in situ hybridization, genomic regions covering one
542 exon or full-length cDNA were PCR amplified to generate fragments with restriction enzyme
543 overhangs. The sequences of all oligos were included in Supplementary table 1. The fragments
544 were inserted to the pBluescript SK(II) vector. In vitro transcription was performed as
545 previously described (He et al., 2021). The mouse brains at defined ages were dissected and
546 fixed for 12 hours in 4% PFA, dehydrated in 25% sucrose, cryoprotected and embedded in
547 O.C.T. The brain samples were then sectioned at 18 μm thickness on Leica cryostats CM3050s.
548 RNA *in situ* hybridization was performed using digoxigenin-labeled riboprobes as described
549 previously. Detailed protocols are available upon request. Images were taken using a Leica
550 DMLB microscope.

551 **Immunostaining**

552 Immunostaining was performed according to standard protocols as previously used [63]. For EdU
553 and BrdU labeling, EdU (5-ethynyl-2′-deoxyuridine) and BrdU (5-bromo-2'-deoxyuridine) (5-
554 20 μg/g of body weight) were injected into the peritoneal cavity of pregnant mice at desired
555 ages. EdU incorporation was detected with the Click-iT assay (Invitrogen) according to the
556 manufacturer's instructions. BrdU incorporation was measured by immunostaining using an
557 antibody against rat-BrdU (Abcam). Imaging was taken on a Zeiss confocal microscope. ZEN
558 (ZeissLSM800), ImageJ (NIH) and Photoshop (Adobe) were used for analysis and
559 quantification.

560 **NSC culture**

561 Control and mutant embryonic cortices from E13.5 animals were dissected and dissociated into
562 single cell suspension and digested with Accutase (Sigma). Cells were maintained in

563 proliferation media (STEMCELL Technologies). Lentivirus expressing Flag-*Prdm16* and a
564 puromycin resistant gene in the pCDH vector was produced in 293J4 cells and used to infect a
565 wild-type NSC line derived from E13.5 forebrain, and the selected NSCs were maintained in
566 puromycin-containing medium for three passages before puromycin withdrawal.

567 **RT-qPCR**

568 *Prdm16_OE*, wild-type and mutant NSCs were cultured and treated with or without BMP4
569 (Sigma). After 48-hour treatment, total RNAs were extracted using TRIzol reagent (Invitrogen).
570 Total RNA was further cleaned with Turbo DNase (Ambion) and used in reverse-transcription
571 with RT master mix (ThermoFisher). To ensure the absence of genomic DNA, control qPCR
572 was performed on the mock-reverse-transcribed RNA samples. The list of qPCR primers is
573 included in supplementary table 1.

574 **SCRINSHOT**

575 Brain sections were prepared in the same way as for regular *in situ* hybridization (described
576 above). The SCRINSHOT experiments were carried out according to the published method [45].
577 In brief, 3 padlock probes and 3 corresponding detection probes were designed for each gene
578 of interest. The slides with cryo-sectioned brain slices were pretreated at 45˚C to reduce
579 moisture and fixed in 4% PFA in 1X PBS, followed by washing in PBS Tween-20 0.05% twice.
580 Permeabilization of tissues were done by washing slides in 0.1M HCl for 2mins 15s, followed
581 by washing in PBS Tween-20 0.05% twice. Then a stepwise dehydration was performed for the
582 slides in 70%, 85% & 100% Ethanol and air. The SecureSeal hybridization chamber (GRACE
583 BIO-LABS, 621501) was then mounted to cover each pair of control and *Prdm16* mutant brain
584 slices. Samples were then blocked in a probe-free hybridization reaction mixture of
585 1XAmplifase buffer (Lucigen, A1905B), 0.05M KCl, 20% Formamide deionized (Millipore
586 S4117), 0.1uM Oligo-dT, 0.1ug/ul BSA (New England Biolabs, B9000S), 1U/ul RiboLock
587 (Thermo, EO0384), and 0.2ug/ul tRNAs (Ambion, AM7119). Then hybridization of padlock
588 probes was done by incubating samples with padlock probes (with the concentration of each
589 one 0.01uM) mixed in blocking reagents used before (no oligo dT used in this step). The slide
590 was then put into a PCR machine to denature at 55˚C for 15 minutes and hybridize at 45˚C for
591 120 minutes. Padlock probes were then ligated by using SplintR ligase (NEB M0375) at 25˚C
592 for 16 hours followed by RCA (rolling cycle amplification) at 30˚C for 16 hours by using phi29
593 polymerase (Lucigen, 30221–2) and RCA primer1. Then a fixation step was applied to stabilize

594 RCA product in 4% PFA for 15 minutes followed by washing in PBS Tween-20 0.05%. Then
595 the hybridization of the first 3 genes was done by mixing all 3 3' fluorophore-conjugated
596 detection probes of each gene in reaction reagent (2XSSC, 20% Formamide deionized, 0.1ug/ul
597 BSA, and 0.5 ng/µl DAPI (Biolegend, 422801) followed by hybridization at 30˚C for 1 hour.
598 The slides were washed in 20% formamide in 2X SSC and then in 6X SSC, followed by
599 dehydration in 70%, 85%, 100% Ethanol until the chamber was removed. Then the samples
600 were preserved in SlowFade Gold Antifade mountant (Thermo, S36936) and kept in dark before
601 imaging. After image acquisition, the first 3 detection probes were removed by using Uracil-
602 DNA Glycosylase (Thermo, EN0362), and the slides were ready for the next round of detection
603 probe hybridization. The procedure was repeated until all genes were hybridized and imaged.

604 Images were acquired with Zeiss Axio Observer 7 fluorescent microscope with an automated
605 stage setting to fix imaging region for different hybridization rounds. Image analysis was done
606 according to the published method [45]. In brief, the DAPI channel from each round was extracted
607 to measure the shift of imaging. The images were then aligned for all gene channels in Zen by
608 Creating Image Subset with the shifting value. After alignment, images were exported into TIFF
609 files and the threshold analysis was carried out for individual channel one by one in CellProfiler
610 with scripts provided by the published method (Alexandros et al. 2020). Then nuclear
611 segmentation was done manually in Fiji ROI manager to obtain nuclear ROIs, followed by an
612 expansion of 2 um in CellProfiler to obtain cell ROIs. Then signal dots were count in these cell
613 ROIs for each gene in CellProfiler and Fiji. Summary of the dot counts for each gene was
614 exported to Excel files.

615 **CUT&TAG**

616 CUT&TAG was performed according to the published method [64]. In brief, *Prdm16_OE* and
617 *Prdm16* mutant NSCs were cultured in NeuroCult™ Proliferation Kit (Stem cell technologies,
618 05702) for 3 days with or without BMP4 at concentration of 25ng/ml medium (Sigma, H4916).
619 Cells on day 3 were then shortly rinsed with 1X PBS and resuspended in 1ml cold NE1 buffer
620 on ice. Nuclei were lightly fixed with 0.1% formaldehyde to 1ml PBS at RT for 2 minutes and
621 neutralized with 75mM Glycine. Nuclei were then washed for 3 times, resuspended in 1mL
622 wash buffer and mixed with 90uL Concanavalin A-coated magnetic beads (Polyscience 86057).
623 The nuclei/beads mix was then blocked with 800 uL cold Antibody buffer for 5 minutes and
624 resuspended in 1.2 mL Antibody buffer and aliquoted into 8 tubes with 150 uL each. 2 uL Anti-
625 PRDM16 (Generous gift from Bryan Bjork lab) or IgG (SIGMA-ALDRICH, I5006) was added

626 into each tube for an overnight incubation at 4°C. The beads/nuclei/antibody mix was then
627 washed with Dig-wash buffer and incubated with secondary antibody (1:100 dilution) for 1
628 hour. After further washes with the Dig-wash buffer. a pA-Tn5 adaptor complex in Dig-300
629 buffer was added to the beads for 1 hour reaction. The beads were then washed with Dig-300
630 buffer before the incubation with 300ul Tagmentation buffer at 37°C for 1 hour. Then 10ul
631 0.5M EDTA, 3uL 10% SDS and 2.5uL 20 mg/mL proteinase K (Invitrogen) were used to stop
632 the reaction. Then the resultant DNA was purified with DNA clean & Concentrator kit (ZYMO
633 Research D4013) and eluted in 25uL Elution buffer. To generate libraries, 21uL fragment DNA
634 was mixed with 2uL 10uM Universal i5 primer, 2uL 10uM uniquely barcoded i7 primer and
635 25uL PCR master mix (NEB Phusion® High-Fidelity PCR Master Mix with HF Buffer,
636 M0531). The PCR condition was as follows: 72°C 5min, 98°C 30s, repeat 12 times (98°C 10s,
637 63°C 10s), 72°C 1 min and hold 4°C. The libraries were cleaned with standard Ampure XP
638 beads as previously described. Libraries from four biological replicates were produced for each
639 condition.

640 **ChIP**

641 ChIP was performed as previously described [65]. For each ChIP reaction, 10 million *Prdm16_OE*,
642 Prdm16_KO NSCs with or without 3-day BMP4 treatment were fixed, lysed, sonicated and
643 made into chromatin extract. After precleared with gamma-bind-G beads, the chromatin extract
644 was incubated with 2ug PRDM16, 2ug SMAD4 (Proteintech, 10231-1-AP), 2ug pSMAD1/5/8
645 (Millipore, AB3848-1) or 2ug SMAD3 (abcam, ab227223) in each ChIP reaction. In sequential
646 ChIP assays, the same chromatin lysate was precleared and used, but with more antibodies in
647 each reaction: 5 ug of IgG or PRDM16 antibody in the first round of immunoprecipitation. The
648 elutes were then precleared again using gamma-bind G beads, divided into two equal halves
649 and immunoprecipitated with 2 ug of IgG or the SMAD4 antibody. In ChIP-qPCR experiments,
650 2ug SMAD4 and 2 ug c-FOS antibodies (Invitrogen, MA5-15055) were used in each reaction.
651 The precipitated DNA was reverse cross-linked, and then purified using the Qiagen PCR
652 purification kit.

653 **Computation analyses**

654 **ChIP-seq libraries and analyses.** 0.2% input and ChIPed DNA were made into libraries using
655 the NEBNext Ultra™ II DNA Library Prep Kit and sequenced on the Illumina Nextseq500
656 platform. Three replicates of ChIP-seq samples, after the adaptor trimming by Trimmomatic,

657 were mapped to the UCSC *Mus musculus* (mm10) genome assembly using Bowtie2 with the
658 default parameters. The uniquely mapped reads (with mapping quality >= 20) were used for
659 further analyses. The peaks were called by HOMER (v4.10) [66]. The reproducibility between
660 replicates was estimated by Irreproducibility Discovery Rate (IDR), using the HOMER IDR
661 pipeline (https://github.com/karmel/homer-idr). As suggested by the Encode IDR guideline, we
662 used a relatively relaxed parameter "-F 2 -fdr 0.3 -P .1 -L 3 -LP .1" for the true/pseudo/pooled
663 replicates by the HOMER peak calling. The final confident peaks were determined by an IDR
664 < 5%. The peaks that were overlapped with mm10 blacklist were also removed.

665 **CUT&TAG analyses.** The CUT&TAG samples of *Prdm16_OE* and *Prdm16* mutant NSCs in
666 four replicates, and of Prdm16 from CH and ChP area at stage 12.5 embryos in three replicates,
667 were mapped to mm10 genome assembly using Bowtie2 (bowtie2 --end-to-end --very-sensitive
668 --no-mixed --no-discordant --phred33 -I 10 -X 700). The CUT&TAG coverage for these
669 samples were generated by bedtools genomeCoverageBed and normalized to the library depths
670 to give a read per million per base (RPM). By using the peak caller SEACR [33], which was
671 designed for calling peaks from sparse chromatin profiling data such as CUT&TAG [22], we
672 performed peak calling with FDR < 10% for each replicated sample (SEACR_1.3.sh
673 normalized_coverage 0.1 non stringent output_peaks). To identify confident peaks, we selected
674 the common peaks, which were called from all replicates for each condition. Peak overlapping
675 analysis was performed by Homer mergePeaks function with default parameters. Peak overlap
676 analysis utilized HOMER's mergePeaks function, specifically employing the default '-d given'
677 parameter. This approach ensures that only peaks directly overlapping with each other are
678 merged, maintaining the precise distances between peaks as provided in the input peak calls.
679 This method is particularly beneficial for retaining the integrity of the original peak boundaries,
680 avoiding any alterations to their relative positions. *De novo* motif discovery from SMAD4 and
681 pSMAD1/5/8 peaks in *Prdm16_OE* NSCs and Prdm16 mutant NSCs were performed by
682 MEME-ChIP software [67] (parameters: -ccut 100 -meme-p 5 -dna -meme-mod anr -minw 5 -
683 maxw 15 -filter-thresh 0.05).

684 The CUT&TAG samples of H3K4me3 BMP4-treated and non-treated *Prdm16_OE* and
685 *Prdm16*_KO cells in 2 or 3 replicates were mapped to mm10 genome assembly using Bowtie2
686 (bowtie2 --end-to-end --very-sensitive --no-mixed --no-discordant --phred33 -I 10 -X 700).
687 Differential analysis of TSS up-stream and down-stream 500 bp between *Prdm16_OE* BMP-
688 treated vs non-BMP-treated and Prdm16_KO vs *Prdm16_OE* BMP-treated were performed by

689 Limma R package [68]. Gene Ontology (GO) enrichment analysis of up-regulated and down-
690 regulated regions was performed by PANTHER [69].

691 **scRNA-seq analyses.** The scRNA-seq data of the developing mouse brain were obtained from
692 [41]. The counts per cell were normalized by logNormCounts function in Bioconductor package
693 "scater" and the normalized expression data per cell were used to generate gene expression
694 violin plots. To test whether Prdm16 target gene sets of Prdm16 with and without BMP4 and
695 ChP E12.5 are significantly enriched among the scRNA-seq gene mean expression in each
696 identified cell type cluster, the gene set enrichment analysis (GESA) "fgesa" Bioconductor
697 package was used [ref: Korotkevich G. et al. Fast gene set enrichment analysis. bioRxiv, 2021.
698 http://biorxiv.org/content/early/2016/06/20/060012].

699 **Acknowledgements**

700 We thank the animal experimental core facility and the imaging facility of Stockholm
701 University and Bioinformatics and Expression analysis core facility at Karolinska Institute,
702 Sweden, for their service and support. We thank Christos Samakovlis and his lab members for
703 technical help on SCRINSHOT experiments. We also appreciate technical help from Adrian
704 Martinez Martin. J.W. is funded by Australian Research Council Centre of Excellence for the
705 Mathematical Analysis of Cellular Systems (CE230100001) and ANU Future Scheme. The
706 project was supported by the research project grant from Swedish Research Council
707 (Vetenskapsrådet, 2020-03543) and the research grants from Swedish Cancerfonden (CAN
708 2017/529 and 20 1046 PjF 01 H) to Q.D.

709 **Author contributions**

710 Q.D. conceived and designed the project. L.H. performed all of the experiments. J.W performed
711 all computational analysis. Q.D., J.W. and L.H. analysed and interpreted the data. Q.D. wrote
712 the manuscript with input from L.H. and J.W.

713 **Data availability**: The CUT&TAG and ChIP-seq data produced in this study have been
714 deposited to Gene Expression Omnibus (GEO accession number: GSE275758).

715

716

717 **Reference:**

718 1. Mira, H., Andreu, Z., Suh, H., Lie, D.C., Jessberger, S., Consiglio, A., San Emeterio, J.,
719 Hortiguela, R., Marques-Torrejon, M.A., Nakashima, K., et al. (2010). Signaling
720 through BMPR-IA regulates quiescence and long-term activity of neural stem cells in
721 the adult hippocampus. Cell Stem Cell *7*, 78-89. 10.1016/j.stem.2010.04.016.
722 2. Colak, D., Mori, T., Brill, M.S., Pfeifer, A., Falk, S., Deng, C., Monteiro, R., Mummery,
723 C., Sommer, L., and Gotz, M. (2008). Adult neurogenesis requires Smad4-mediated
724 bone morphogenic protein signaling in stem cells. J Neurosci *28*, 434-446.
725 10.1523/JNEUROSCI.4374-07.2008.
726 3. Zhang, L., Ye, Y., Long, X., Xiao, P., Ren, X., and Yu, J. (2016). BMP signaling and its
727 paradoxical effects in tumorigenesis and dissemination. Oncotarget *7*, 78206-78218.
728 10.18632/oncotarget.12151.
729 4. Zhang, J., and Li, L. (2005). BMP signaling and stem cell regulation. Dev Biol *284*, 1-11.
730 10.1016/j.ydbio.2005.05.009.
731 5. Hogan, B.L. (1996). Bone morphogenetic proteins: multifunctional regulators of
732 vertebrate development. Genes & development *10*, 1580-1594.
733 10.1101/gad.10.13.1580.
734 6. Massague, J. (1998). TGF-beta signal transduction. Annu Rev Biochem *67*, 753-791.
735 10.1146/annurev.biochem.67.1.753.
736 7. Martin-Malpartida, P., Batet, M., Kaczmarska, Z., Freier, R., Gomes, T., Aragon, E.,
737 Zou, Y., Wang, Q., Xi, Q., Ruiz, L., et al. (2017). Structural basis for genome wide
738 recognition of 5-bp GC motifs by SMAD transcription factors. Nat Commun *8*, 2070.
739 10.1038/s41467-017-02054-6.
740 8. Hill, C.S. (2016). Transcriptional Control by the SMADs. Cold Spring Harb Perspect Biol
741 *8*. 10.1101/cshperspect.a022079.
742 9. Liddelow, S.A., Dziegielewska, K.M., Vandeberg, J.L., and Saunders, N.R. (2010).
743 Development of the lateral ventricular choroid plexus in a marsupial, Monodelphis
744 domestica. Cerebrospinal Fluid Res *7*, 16. 10.1186/1743-8454-7-16.
745 10. Hebert, J.M., Mishina, Y., and McConnell, S.K. (2002). BMP signaling is required
746 locally to pattern the dorsal telencephalic midline. Neuron *35*, 1029-1041.
747 10.1016/s0896-6273(02)00900-5.
748 11. Watanabe, M., Kang, Y.J., Davies, L.M., Meghpara, S., Lau, K., Chung, C.Y., Kathiriya,
749 J., Hadjantonakis, A.K., and Monuki, E.S. (2012). BMP4 sufficiency to induce choroid
750 plexus epithelial fate from embryonic stem cell-derived neuroepithelial progenitors. J
751 Neurosci *32*, 15934-15945. 10.1523/JNEUROSCI.3227-12.2012.
752 12. Parichha, A., Suresh, V., Chatterjee, M., Kshirsagar, A., Ben-Reuven, L., Olender, T.,
753 Taketo, M.M., Radosevic, V., Bobic-Rasonja, M., Trnski, S., et al. (2022). Constitutive
754 activation of canonical Wnt signaling disrupts choroid plexus epithelial fate. Nat
755 Commun *13*, 633. 10.1038/s41467-021-27602-z.
756 13. Aguilo, F., Avagyan, S., Labar, A., Sevilla, A., Lee, D.F., Kumar, P., Lemischka, I.R.,
757 Zhou, B.Y., and Snoeck, H.W. (2011). Prdm16 is a physiologic regulator of
758 hematopoietic stem cells. Blood *117*, 5057-5066. 10.1182/blood-2010-08-300145.
759 14. Chuikov, S., Levi, B.P., Smith, M.L., and Morrison, S.J. (2010). Prdm16 promotes stem
760 cell maintenance in multiple tissues, partly by regulating oxidative stress. Nat Cell
761 Biol *12*, 999-1006. 10.1038/ncb2101.

762 15. Kajimura, S., Seale, P., Tomaru, T., Erdjument-Bromage, H., Cooper, M.P., Ruas, J.L.,
763 Chin, S., Tempst, P., Lazar, M.A., and Spiegelman, B.M. (2008). Regulation of the
764 brown and white fat gene programs through a PRDM16/CtBP transcriptional
765 complex. Genes & development *22*, 1397-1409. 10.1101/gad.1666108.
766 16. Shimada, I.S., Acar, M., Burgess, R.J., Zhao, Z., and Morrison, S.J. (2017). Prdm16 is
767 required for the maintenance of neural stem cells in the postnatal forebrain and their
768 differentiation into ependymal cells. Genes & development *31*, 1134-1146.
769 10.1101/gad.291773.116.
770 17. Chui, A., Zhang, Q., Dai, Q., and Shi, S.H. (2020). Oxidative stress regulates progenitor
771 behavior and cortical neurogenesis. Development *147*. 10.1242/dev.184150.
772 18. Baizabal, J.M., Mistry, M., Garcia, M.T., Gomez, N., Olukoya, O., Tran, D., Johnson,
773 M.B., Walsh, C.A., and Harwell, C.C. (2018). The Epigenetic State of PRDM16-
774 Regulated Enhancers in Radial Glia Controls Cortical Neuron Position. Neuron *98*,
775 945-962 e948. 10.1016/j.neuron.2018.04.033.
776 19. Inoue, M., Iwai, R., Tabata, H., Konno, D., Komabayashi-Suzuki, M., Watanabe, C.,
777 Iwanari, H., Mochizuki, Y., Hamakubo, T., Matsuzaki, F., et al. (2017). Prdm16 is
778 crucial for progression of the multipolar phase during neural differentiation of the
779 developing neocortex. Development *144*, 385-399. 10.1242/dev.136382.
780 20. He, L., Jones, J., He, W., Bjork, B.C., Wen, J., and Dai, Q. (2021). PRDM16 regulates a
781 temporal transcriptional program to promote progression of cortical neural
782 progenitors. Development *148*. 10.1242/dev.194670.
783 21. Bjork, B.C., Turbe-Doan, A., Prysak, M., Herron, B.J., and Beier, D.R. (2010). Prdm16 is
784 required for normal palatogenesis in mice. Hum Mol Genet *19*, 774-789.
785 10.1093/hmg/ddp543.
786 22. Strassman, A., Schnutgen, F., Dai, Q., Jones, J.C., Gomez, A.C., Pitstick, L., Holton,
787 N.E., Moskal, R., Leslie, E.R., von Melchner, H., et al. (2017). Generation of a
788 multipurpose Prdm16 mouse allele by targeted gene trapping. Dis Model Mech *10*,
789 909-922. 10.1242/dmm.029561.
790 23. Warner, D.R., Horn, K.H., Mudd, L., Webb, C.L., Greene, R.M., and Pisano, M.M.
791 (2007). PRDM16/MEL1: a novel Smad binding protein expressed in murine embryonic
792 orofacial tissue. Biochim Biophys Acta *1773*, 814-820. 10.1016/j.bbamcr.2007.03.016.
793 24. Seale, P., Kajimura, S., Yang, W., Chin, S., Rohas, L.M., Uldry, M., Tavernier, G., Langin,
794 D., and Spiegelman, B.M. (2007). Transcriptional control of brown fat determination
795 by PRDM16. Cell Metab *6*, 38-54. 10.1016/j.cmet.2007.06.001.
796 25. Tseng, Y.H., Kokkotou, E., Schulz, T.J., Huang, T.L., Winnay, J.N., Taniguchi, C.M., Tran,
797 T.T., Suzuki, R., Espinoza, D.O., Yamamoto, Y., et al. (2008). New role of bone
798 morphogenetic protein 7 in brown adipogenesis and energy expenditure. Nature
799 *454*, 1000-1004. 10.1038/nature07221.
800 26. Shull, L.C., Lencer, E.S., Kim, H.M., Goyama, S., Kurokawa, M., Costello, J.C., Jones, K.,
801 and Artinger, K.B. (2022). PRDM paralogs antagonistically balance Wnt/beta-catenin
802 activity during craniofacial chondrocyte differentiation. Development *149*.
803 10.1242/dev.200082.
804 27. Arndt, A.K., Schafer, S., Drenckhahn, J.D., Sabeh, M.K., Plovie, E.R., Caliebe, A.,
805 Klopocki, E., Musso, G., Werdich, A.A., Kalwa, H., et al. (2013). Fine mapping of the
806 1p36 deletion syndrome identifies mutation of PRDM16 as a cause of
807 cardiomyopathy. Am J Hum Genet *93*, 67-77. 10.1016/j.ajhg.2013.05.015.

808 28. Hu, J.S., Doan, L.T., Currle, D.S., Paff, M., Rheem, J.Y., Schreyer, R., Robert, B., and
809 Monuki, E.S. (2008). Border formation in a Bmp gradient reduced to single
810 dissociated cells. Proc Natl Acad Sci U S A *105*, 3398-3403.
811 10.1073/pnas.0709100105.
812 29. Wang, Q., Li, H., Tajima, K., Verkerke, A.R.P., Taxin, Z.H., Hou, Z., Cole, J.B., Li, F.,
813 Wong, J., Abe, I., et al. (2022). Post-translational control of beige fat biogenesis by
814 PRDM16 stabilization. Nature *609*, 151-158. 10.1038/s41586-022-05067-4.
815 30. Benayoun, B.A., Pollina, E.A., Ucar, D., Mahmoudi, S., Karra, K., Wong, E.D.,
816 Devarajan, K., Daugherty, A.C., Kundaje, A.B., Mancini, E., et al. (2014). H3K4me3
817 breadth is linked to cell identity and transcriptional consistency. Cell *158*, 673-688.
818 10.1016/j.cell.2014.06.027.
819 31. Katada, S., Takouda, J., Nakagawa, T., Honda, M., Igarashi, K., Imamura, T., Ohkawa,
820 Y., Sato, S., Kurumizaka, H., and Nakashima, K. (2021). Neural stem/precursor cells
821 dynamically change their epigenetic landscape to differentially respond to BMP
822 signaling for fate switching during brain development. Genes & development *35*,
823 1431-1444. 10.1101/gad.348797.121.
824 32. Tooley, J., and Stukenberg, P.T. (2011). The Ndc80 complex: integrating the
825 kinetochore's many movements. Chromosome Res *19*, 377-391. 10.1007/s10577-
826 010-9180-5.
827 33. Meers, M.P., Tenenbaum, D., and Henikoff, S. (2019). Peak calling by Sparse
828 Enrichment Analysis for CUT&RUN chromatin profiling. Epigenetics Chromatin *12*, 42.
829 10.1186/s13072-019-0287-4.
830 34. Zawel, L., Dai, J.L., Buckhaults, P., Zhou, S., Kinzler, K.W., Vogelstein, B., and Kern, S.E.
831 (1998). Human Smad3 and Smad4 are sequence-specific transcription activators. Mol
832 Cell *1*, 611-617. 10.1016/s1097-2765(00)80061-1.
833 35. Dennler, S., Itoh, S., Vivien, D., ten Dijke, P., Huet, S., and Gauthier, J.M. (1998).
834 Direct binding of Smad3 and Smad4 to critical TGF beta-inducible elements in the
835 promoter of human plasminogen activator inhibitor-type 1 gene. EMBO J *17*, 3091-
836 3100. 10.1093/emboj/17.11.3091.
837 36. Wong, C., Rougier-Chapman, E.M., Frederick, J.P., Datto, M.B., Liberati, N.T., Li, J.M.,
838 and Wang, X.F. (1999). Smad3-Smad4 and AP-1 complexes synergize in
839 transcriptional activation of the c-Jun promoter by transforming growth factor beta.
840 Mol Cell Biol *19*, 1821-1830. 10.1128/MCB.19.3.1821.
841 37. Pyrowolakis, G., Hartmann, B., Muller, B., Basler, K., and Affolter, M. (2004). A simple
842 molecular complex mediates widespread BMP-induced repression during Drosophila
843 development. Dev Cell *7*, 229-240. 10.1016/j.devcel.2004.07.008.
844 38. Gao, S., Steffen, J., and Laughon, A. (2005). Dpp-responsive silencers are bound by a
845 trimeric Mad-Medea complex. J Biol Chem *280*, 36158-36164.
846 10.1074/jbc.M506882200.
847 39. Weiss, A., Charbonnier, E., Ellertsdottir, E., Tsirigos, A., Wolf, C., Schuh, R.,
848 Pyrowolakis, G., and Affolter, M. (2010). A conserved activation element in BMP
849 signaling during Drosophila development. Nat Struct Mol Biol *17*, 69-76.
850 10.1038/nsmb.1715.
851 40. Zhang, Y., Feng, X.H., and Derynck, R. (1998). Smad3 and Smad4 cooperate with c-
852 Jun/c-Fos to mediate TGF-beta-induced transcription. Nature *394*, 909-913.
853 10.1038/29814.

854 41. La Manno, G., Siletti, K., Furlan, A., Gyllborg, D., Vinsland, E., Mossi Albiach, A.,
855 Mattsson Langseth, C., Khven, I., Lederer, A.R., Dratva, L.M., et al. (2021). Molecular
856 architecture of the developing mouse brain. Nature *596*, 92-96. 10.1038/s41586-021-
857 03775-x.
858 42. Rhodes, C.T., Thompson, J.J., Mitra, A., Asokumar, D., Lee, D.R., Lee, D.J., Zhang, Y.,
859 Jason, E., Dale, R.K., Rocha, P.P., and Petros, T.J. (2022). An epigenome atlas of neural
860 progenitors within the embryonic mouse forebrain. Nat Commun *13*, 4196.
861 10.1038/s41467-022-31793-4.
862 43. Kalani, M.Y., Cheshier, S.H., Cord, B.J., Bababeygy, S.R., Vogel, H., Weissman, I.L.,
863 Palmer, T.D., and Nusse, R. (2008). Wnt-mediated self-renewal of neural
864 stem/progenitor cells. Proc Natl Acad Sci U S A *105*, 16970-16975.
865 10.1073/pnas.0808616105.
866 44. Harrison-Uy, S.J., and Pleasure, S.J. (2012). Wnt signaling and forebrain development.
867 Cold Spring Harb Perspect Biol *4*, a008094. 10.1101/cshperspect.a008094.
868 45. Sountoulidis, A., Liontos, A., Nguyen, H.P., Firsova, A.B., Fysikopoulos, A., Qian, X.,
869 Seeger, W., Sundstrom, E., Nilsson, M., and Samakovlis, C. (2020). SCRINSHOT
870 enables spatial mapping of cell states in tissue sections with single-cell resolution.
871 PLoS Biol *18*, e3000675. 10.1371/journal.pbio.3000675.
872 46. Itasaki, N., and Hoppler, S. (2010). Crosstalk between Wnt and bone morphogenic
873 protein signaling: a turbulent relationship. Dev Dyn *239*, 16-33. 10.1002/dvdy.22009.
874 47. Pellegrini, L., Bonfio, C., Chadwick, J., Begum, F., Skehel, M., and Lancaster, M.A.
875 (2020). Human CNS barrier-forming organoids with cerebrospinal fluid production.
876 Science *369*. 10.1126/science.aaz5626.
877 48. Takahata, M., Inoue, Y., Tsuda, H., Imoto, I., Koinuma, D., Hayashi, M., Ichikura, T.,
878 Yamori, T., Nagasaki, K., Yoshida, M., et al. (2009). SKI and MEL1 cooperate to inhibit
879 transforming growth factor-beta signal in gastric cancer cells. J Biol Chem *284*, 3334-
880 3344. 10.1074/jbc.M808989200.
881 49. Hurwitz, E., Parajuli, P., Ozkan, S., Prunier, C., Nguyen, T.L., Campbell, D., Friend, C.,
882 Bryan, A.A., Lu, T.X., Smith, S.C., et al. (2023). Antagonism between Prdm16 and
883 Smad4 specifies the trajectory and progression of pancreatic cancer. J Cell Biol *222*.
884 10.1083/jcb.202203036.
885 50. Wu, M., Chen, G., and Li, Y.P. (2016). TGF-beta and BMP signaling in osteoblast,
886 skeletal development, and bone formation, homeostasis and disease. Bone Res *4*,
887 16009. 10.1038/boneres.2016.9.
888 51. Nie, X., Luukko, K., and Kettunen, P. (2006). BMP signalling in craniofacial
889 development. Int J Dev Biol *50*, 511-521. 10.1387/ijdb.052101xn.
890 52. van Wijk, B., Moorman, A.F., and van den Hoff, M.J. (2007). Role of bone
891 morphogenetic proteins in cardiac differentiation. Cardiovasc Res *74*, 244-255.
892 10.1016/j.cardiores.2006.11.022.
893 53. Gessert, S., and Kuhl, M. (2010). The multiple phases and faces of wnt signaling
894 during cardiac differentiation and development. Circ Res *107*, 186-199.
895 10.1161/CIRCRESAHA.110.221531.
896 54. Geetha-Loganathan, P., Nimmagadda, S., and Scaal, M. (2008). Wnt signaling in limb
897 organogenesis. Organogenesis *4*, 109-115. 10.4161/org.4.2.5857.
898 55. Robert, B. (2007). Bone morphogenetic protein signaling in limb outgrowth and
899 patterning. Dev Growth Differ *49*, 455-468. 10.1111/j.1440-169X.2007.00946.x.

900 56. Stine, R.R., Sakers, A.P., TeSlaa, T., Kissig, M., Stine, Z.E., Kwon, C.W., Cheng, L., Lim,
901 H.W., Kaestner, K.H., Rabinowitz, J.D., and Seale, P. (2019). PRDM16 Maintains
902 Homeostasis of the Intestinal Epithelium by Controlling Region-Specific Metabolism.
903 Cell Stem Cell *25*, 830-845 e838. 10.1016/j.stem.2019.08.017.
904 57. Korinek, V., Barker, N., Moerer, P., van Donselaar, E., Huls, G., Peters, P.J., and
905 Clevers, H. (1998). Depletion of epithelial stem-cell compartments in the small
906 intestine of mice lacking Tcf-4. Nat Genet *19*, 379-383. 10.1038/1270.
907 58. He, X.C., Zhang, J., Tong, W.G., Tawfik, O., Ross, J., Scoville, D.H., Tian, Q., Zeng, X.,
908 He, X., Wiedemann, L.M., et al. (2004). BMP signaling inhibits intestinal stem cell self-
909 renewal through suppression of Wnt-beta-catenin signaling. Nat Genet *36*, 1117-
910 1121. 10.1038/ng1430.
911 59. Wolff, J.E., Sajedi, M., Brant, R., Coppes, M.J., and Egeler, R.M. (2002). Choroid plexus
912 tumours. Br J Cancer *87*, 1086-1091. 10.1038/sj.bjc.6600609.
913 60. Johansson, P.A. (2014). The choroid plexuses and their impact on developmental
914 neurogenesis. Front Neurosci *8*, 340. 10.3389/fnins.2014.00340.
915 61. Lehtinen, M.K., Bjornsson, C.S., Dymecki, S.M., Gilbertson, R.J., Holtzman, D.M., and
916 Monuki, E.S. (2013). The choroid plexus and cerebrospinal fluid: emerging roles in
917 development, disease, and therapy. J Neurosci *33*, 17553-17559.
918 10.1523/JNEUROSCI.3258-13.2013.
919 62. Lun, M.P., Monuki, E.S., and Lehtinen, M.K. (2015). Development and functions of the
920 choroid plexus-cerebrospinal fluid system. Nat Rev Neurosci *16*, 445-457.
921 10.1038/nrn3921.
922 63. Dai, Q., Andreu-Agullo, C., Insolera, R., Wong, L.C., Shi, S.H., and Lai, E.C. (2013).
923 BEND6 is a nuclear antagonist of Notch signaling during self-renewal of neural stem
924 cells. Development *140*, 1892-1902. 10.1242/dev.087502.
925 64. Kaya-Okur, H.S., Wu, S.J., Codomo, C.A., Pledger, E.S., Bryson, T.D., Henikoff, J.G.,
926 Ahmad, K., and Henikoff, S. (2019). CUT&Tag for efficient epigenomic profiling of
927 small samples and single cells. Nat Commun *10*, 1930. 10.1038/s41467-019-09982-5.
928 65. Dai, Q., Ren, A., Westholm, J.O., Serganov, A.A., Patel, D.J., and Lai, E.C. (2013). The
929 BEN domain is a novel sequence-specific DNA-binding domain conserved in neural
930 transcriptional repressors. Genes & development *27*, 602-614.
931 10.1101/gad.213314.113.
932 66. Heinz, S., Benner, C., Spann, N., Bertolino, E., Lin, Y.C., Laslo, P., Cheng, J.X., Murre,
933 C., Singh, H., and Glass, C.K. (2010). Simple combinations of lineage-determining
934 transcription factors prime cis-regulatory elements required for macrophage and B
935 cell identities. Mol Cell *38*, 576-589. 10.1016/j.molcel.2010.05.004.
936 67. Machanick, P., and Bailey, T.L. (2011). MEME-ChIP: motif analysis of large DNA
937 datasets. Bioinformatics *27*, 1696-1697. 10.1093/bioinformatics/btr189.
938 68. Ritchie, M.E., Phipson, B., Wu, D., Hu, Y., Law, C.W., Shi, W., and Smyth, G.K. (2015).
939 limma powers differential expression analyses for RNA-sequencing and microarray
940 studies. Nucleic Acids Res *43*, e47. 10.1093/nar/gkv007.
941 69. Thomas, P.D., Ebert, D., Muruganujan, A., Mushayahama, T., Albou, L.P., and Mi, H.
942 (2022). PANTHER: Making genome-scale phylogenetics accessible to all. Protein Sci
943 *31*, 8-22. 10.1002/pro.4218.
944

945

946 **Figure legend**

947 **Figure 1. *Prdm16* mutant ChP cells fail to exit the cell cycle and retain neural progenitor**
948 **identity**

949 (**A**) RNA *in situ* hybridization using a *Prdm16* probe shows *Prdm16* expression in E10.5 and
950 E12.5 brains. The line and bracket mark the developing CH and ChP. (**B**) Top: Schematic of
951 the *Prdm16* GT allele**,** as reported in Strassman A. et al, 2017. Bottom: immunostaining of
952 PRDM16 in E13.5 control and null mutant brains. Red: PRDM16; blue: DAPI. White arrows
953 indicate the ChP in the control brain. (**C**) RNA in situ hybridization for *Ttr* on E12.5 control
954 and *Prdm16* null mutant forebrains. Cortical hem (CH) regions are outlined based on
955 morphology. (**D**) Two-hour EdU labeling in E12.5 control and *Prdm16* homozygous brains.
956 Sections are co-stained with anti-*β*-Gal antibody to identify mutant ChP cells in the KO brain.
957 Note: the *β-Geo* trap is absent in wild-type animals. Brackets mark ChP regions. Red: β-Gal;
958 blue: DAPI; green: EdU. (**E**) Immunostaining for DCX on E12.5 control and *Prdm16*
959 homozygous brain slices. Bottom panels show magnified views of the ChP (dashed rectangles).
960 Yellow arrows indicate some of the DCX-positive cells. Right panels show quantification of
961 EdU+ (**D**) and DCX+ cells (**E**). (**F**) Schematic of the double S-phase labeling experiment (top).
962 Brain sections from E14.5 control and prdm16 KO embryos were immunostained with
963 PRDM16 and BrdU antibodies and processed for EdU detection. Bottom panels show
964 magnified views of the ChP region. (**G**) Quantification of EdU+ and BrdU+ cells from the
965 double labeling experiment. Biological replicates: N=3. Error bars represent standard deviation
966 (SD). Statistical significance is calculated using unpaired t-test. ***, $p<0.001$.

967 **Figure 2. *Prdm16* is required for BMP4-induced NSC quiescence**

968 (**A**) Schematic of the NSC culture assay. (**B**) Immunostaining of mKI67 in red and SOX2 in
969 green and EdU labeling in blue on indicated NSC genotypes and treatment. (**C-D**)
970 Quantification of the fraction of mKI67+ (C) and EdU+ (D) cells among the total cell number
971 marked by SOX2. (**E**) RT-qPCR measurement of *Ttr* levels relative to 18S RNAs. Biological
972 replicates: N=3. Error bars represent standard deviation (SD). Statistical significance is
973 calculated using unpaired t-test. ***, $p<0.001$; **, p< 001; *, $p<0.05$; n.s., non-significant.

974 **Figure 3. BMP signaling represses cell proliferation genes to induce cell quiescence**

975 (**A**) Heatmaps of ChIP-seq coverage (normalized by library depths and input) centered at peak
976 summits for SMAD4, pSMAD1/5/8 and SMAD3 in *Prdm16_OE* cells with or without BMP4.
977 (**B**) Volcano plot displaying differential H3K4me3 signal at TSS in *Prdm16_OE* cells with
978 BMP4 versus untreated controls. Genes with significant changes ($P < 0.01$) are colored. (**C**)
979 Bubble plot of GO terms significantly enriched among SMAD-repressed genes (highlighted in
980 dark green in panel B). (**D**) Volcano plot of differential H3K4me3 signal at TSS comparing
981 *Prdm16_KO* and *Prdm16_OE* cells, both treated with BMP4. Significantly changed genes (P
982 < 0.01) are colored. **(E)** Heatmap of normalized H3K4me3 read counts at the TSS of 31 genes
983 co-repressed by PRDM16 and SMADs (overlapping genes from dark green in B and dark pink
984 in D). (**F**) RT-qPCR quantification of *Wnt7b* and *Cdkn1a* mRNA levels across indicated
985 genotypes and treatment conditions. Data represent three biological replicates, each with two
986 technical replicates. Statistical significance was calculated using unpaired t-test (***, p<0.001;
987 **, p< 0.01; *, p<0.05; n.s., non-significant). (**G**) Genome browser tracks of H3K4me3
988 CUT&TAG profiles at the *Wnt7b* and *Cdkn1a* loci.

989 **Figure 4. PRDM16 anchors SMAD proteins at specific genomic regions to mediate gene**
990 **repression**

991 (**A)** Venn diagram showing overlap of PRDM16 CUT&TAG peak in BMP4-treated and un
992 treated *Prdm16_OE* cells. **(B)** Average PRDM16 CUT&Tag signal (normalized to library size)
993 at peak summits in BMP4-treated, untreated Prdm16_OE, and Prdm16_KO cells (4 replicates
994 combined). **(C)** Metaplots of SMAD4 and pSMAD1/5/8 ChIP-seq coverage centered on peak
995 summits with (top) and without (bottom) PRDM16 co-binding in BMP4 treated *Prdm16_OE*
996 and *Prdm16_KO* cells. Bar plots (right) show average coverage; significant reduction in the
997 KO cells is seen only at PRDM16 co-bound sites (*** P<0.001; ** P<0.01; * P<0.05; n.a.
998 P>0.05). **(D-E)** Genome browser view of *Wnt7b* and *Id1* loci showing PRDM16 CUT&TAG
999 and SMAD ChIP-seq tracks. Co-bound regions are highlighted. **(F-G)** ChIP-qPCR validation
1000 of SMAD4 binding at highlighted regions in D-E from *Prdm16_OE* and *Prdm16_KO* cells (2
1001 replicates). (**H**) Frequency of four SMAD motif types across SMAD ChP-seq peaks binned by
1002 binding strength. The palindromic motif GTCTAGAC is most enriched at PRDM16 co-bound
1003 sites (solid red) and notably reduced in non-co-bound peaks (dashed red).

1004 **Figure 5. The SMAD complex shifts genome binding in the absence of Prdm16**

1005 (**A-B**) Genome browser views of the *Id3* (top) and *Wnt7b* (bottom) loci showing ectopic SMAD
1006 peaks (arrows) in *Prdm16 KO* cells. **(C)** Volcano plots showing differential ChIP-seq signal for
1007 SMAD4 and pSMAD1/5/8 in BMP4-treated *Prdm16_KO* cells versus BMP4-treated
1008 *Prdm16_OE* cells. Blue dots represent sites co-bound by PRDM16; red dots indicate sites not
1009 bound by PRDM16 but located within 200kb of a PRDM16-cobound region. Mean log2 fold-
1010 change values are plotted to the right. (**D-E**) *De novo* motif discovery from SMAD4 and
1011 pSMAD1/5/8 ChIP-seq peaks in *Prdm16_OE* cells (**D**) and *Prdm16_KO* cells (**E**). (**F-G**) ChIP-
1012 qPCR validation of increased SMAD4 and c-FOS occupancy at the indicated ectopic binding
1013 sites in *Prdm16_KO* versus *Prdm16_OE* cells. Locations of PCR amplicons are shown in A
1014 and B. **(H)** Model illustrating enhancer switching: in the absence of PRDM16, SMAD
1015 complexes alter their co-factors and function as transcriptional activators.

1016 **Figure 6. PRDM16 and SMADs co-regulated genes exhibit differential expressed in ChP**
1017 **and neural cells**

1018 (**A**) Schematic illustrating the CH and ChP regions, which exhibit opposing Wnt and BMP
1019 signaling gradients. Shown alongside is a violin plot of scRNA-seq expression at E12.5 for the
1020 indicated genes across cell type clusters [37]. Cell clusters were defined based on marker gene
1021 expression from E9.5-E18.5 brain tissues, including choroid plexus clusters 1-5 (Chpl), with
1022 Chpl5 newly identified in this study based on *Ttr* expression as well as radial glia clusters:
1023 RglCH 1-3, RglDF 6-10, and RglF7. CH: cortical hem; DF: dorsal forebrain; F: forebrain. Gene
1024 expression per cell is represented as log2-normalized counts. **(B)** Metaplots and heatmaps
1025 showing CUT&TAG signal for PRDM16 and IgG, centered on peak summits and normalized
1026 for library size, from E12.5 dorsal midline tissues. **(C)** Genome browser view of the *Wnt7b*
1027 locus, displaying CUT&TAG tracks for PRDM16 and ChIP-seq tracks for SMAD proteins.

1028 **Figure 7. PRDM16 suppresses Wnt signaling and cell proliferation in ChP epithelial cells**
1029

1030 (**A**) SCRINSHOT images of E11.5 wild-type and *Prdm16* mutant brains probed for *BMP4*, *Ttr*,
1031 *Wnt7b* and *Wnt2b*. Red arrows indicate autofluorescent blood cells (non-specific signal in all
1032 channels). Cells quantified are circled in yellow, and the red dashed line marks the CH and ChP
1033 boundary. (**B**) Enlarged views of the boxed region in (A), showing increased expression of Wnt
1034 and neural genes and decreased *Ttr* and *Prdm16* in mutants. (**C**) Violin plots displaying dot
1035 counts for the 24 genes in 330 CH and 330 ChP cells from three wild-type and three *Prdm16*
1036 mutant samples. (**D**) SCRINSHOT images of E12.5 wild-type and *Prdm16* mutant brains with

1037 probes for *Axin2*, *Ttr*, *Wnt7b*, *Wnt2b* and *mKi67*. (**E**) Enlarged views of the boxed areas in (D),
1038 with ChP regions outlined by dashed lines. (**F**) Distribution of dot counts for indicated genes in
1039 wild-type (*wt*) and *Prdm16* mutant (*mut*) CH and ChP cells. X-axis: 110 cells per replicate; Y-
1040 axis: mean dot count across three biological replicates. P values calculated using area under the
1041 ROC curve (Prism Graphpad). (**G**) Multi-variant linear regression of *mKi67*, *Axin2* and *Ttr*
1042 expression across 660 CH and ChP cells per genotype. Pearson correlation and significance
1043 were calculated using Prism Graphpad. (**H**) Model illustrating the regulatory circuit through
1044 which PRDM16 promotes the transition from proliferative to quiescent NSCs, a prerequisite
1045 step for ChP epithelial cell specification.
1046
1047
1048

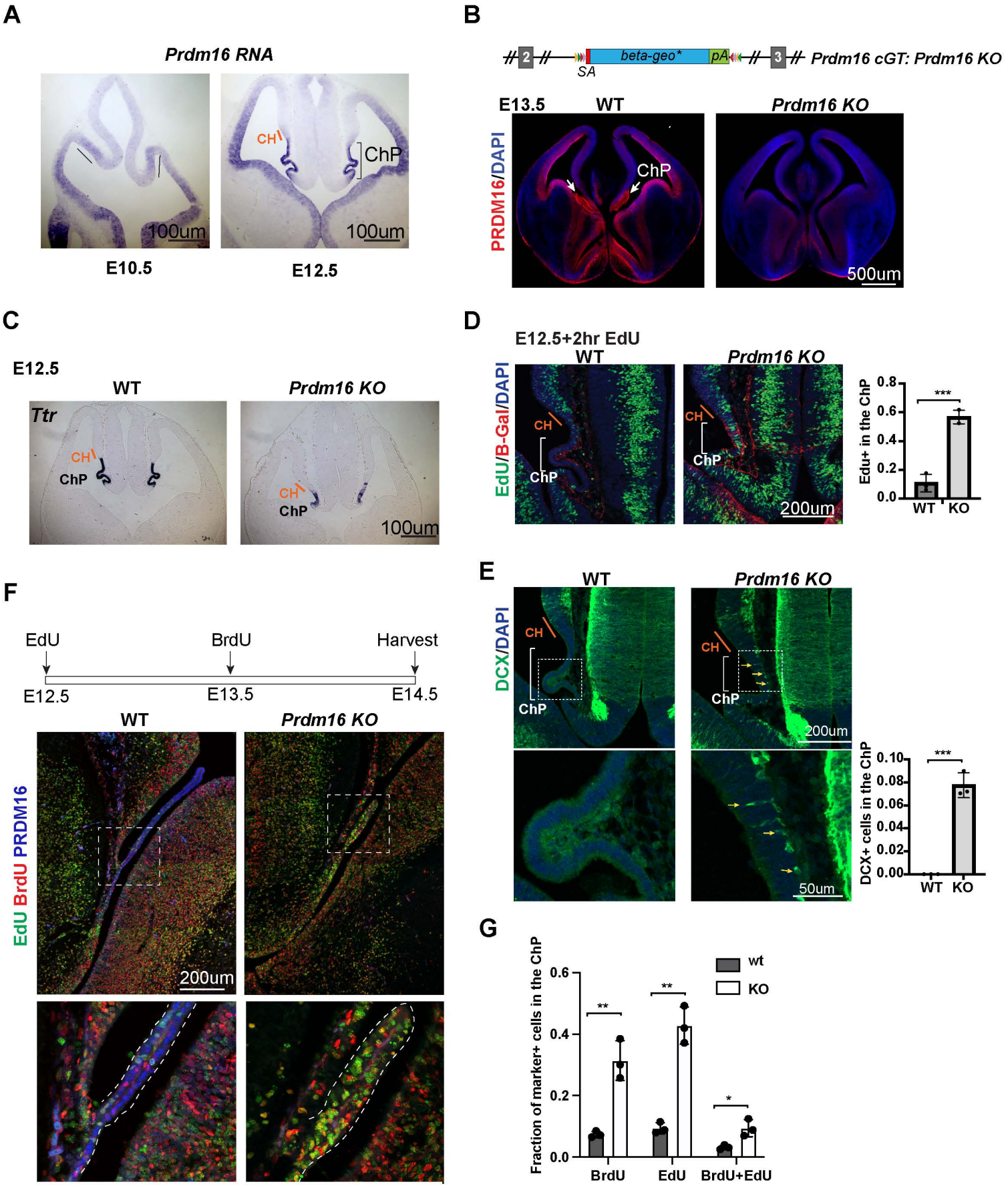
A
Prdm16 RNA
CH
ChP
100um
100um
E10.5
E12.5
B
2
beta-geo*
pA
3
SA
Prdm16 cGT: Prdm16 KO
E13.5
WT
Prdm16 KO
PRDM16/DAPI
ChP
500um
C
E12.5
WT
Prdm16 KO
Ttr
CH
ChP
CH
ChP
100um
D
E12.5+2hr EdU
WT
Prdm16 KO
EdU/B-Gal/DAPI
CH
ChP
CH
ChP
200um
Edu+ in the ChP
0.8
0.6
0.4
0.2
0.0
***
WT
KO
E
WT
Prdm16 KO
DCX/DAPI
CH
ChP
CH
ChP
200um
50um
DCX+ cells in the ChP
0.10
0.08
0.06
0.04
0.02
0.00
***
WT
KO
F
EdU
BrdU
Harvest
E12.5
E13.5
E14.5
WT
Prdm16 KO
EdU BrdU PRDM16
200um
G
Fraction of marker+ cells in the ChP
0.6
0.4
0.2
0.0
wt
KO
**
**
*
BrdU
EdU
BrdU+EdU

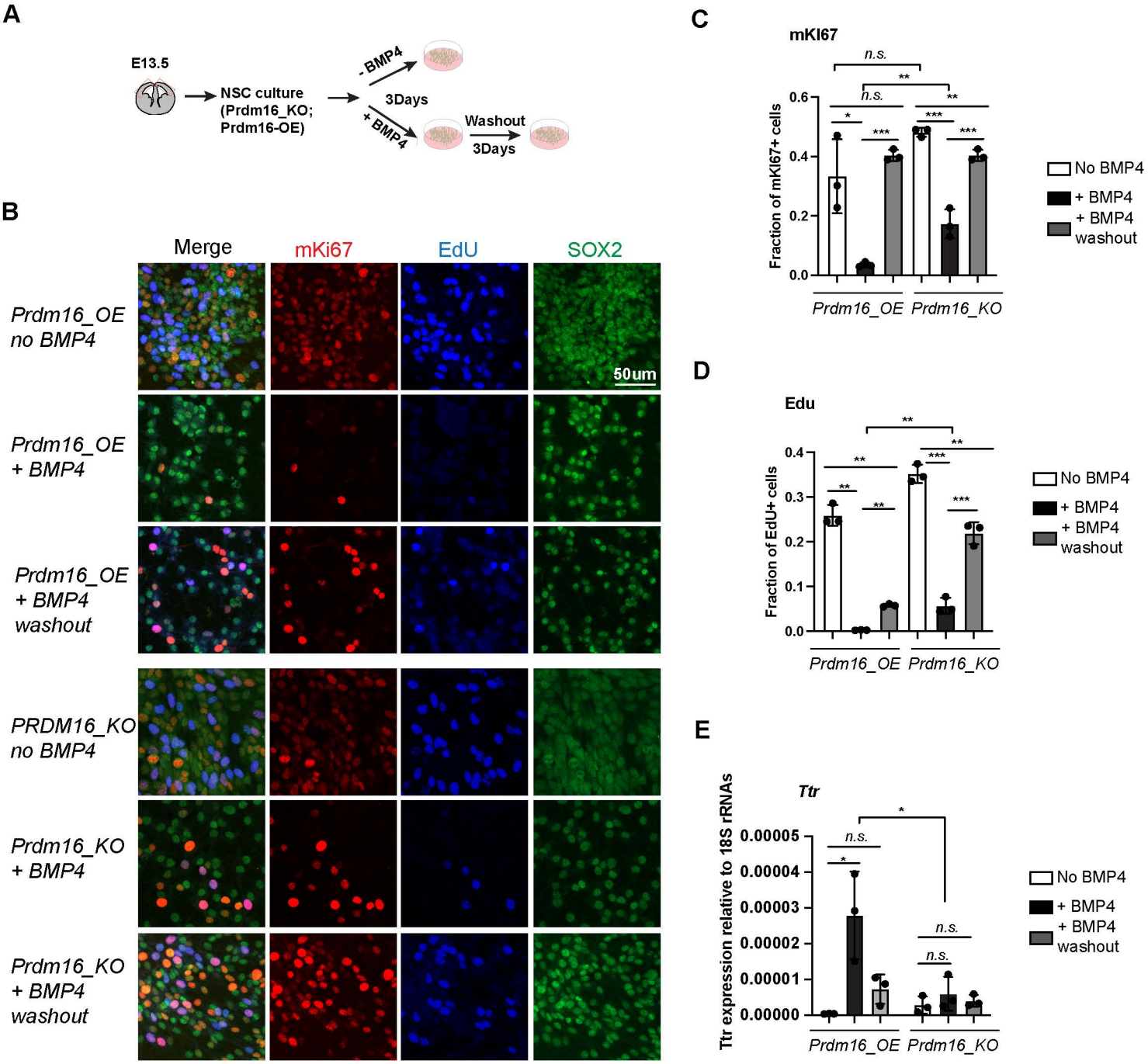
A
E13.5
NSC culture
(Prdm16_KO;
Prdm16-OE)
- BMP4
+ BMP4
3Days
Washout
3Days
B
Merge
mKi67
EdU
SOX2
Prdm16_OE
no BMP4
Prdm16_OE
+ BMP4
Prdm16_OE
+ BMP4
washout
PRDM16_KO
no BMP4
Prdm16_KO
+ BMP4
Prdm16_KO
+ BMP4
washout
50um
C
mKI67
Fraction of mKI67+ cells
Prdm16_OE
Prdm16_KO
No BMP4
+ BMP4
+ BMP4
washout
D
Edu
Fraction of EdU+ cells
Prdm16_OE
Prdm16_KO
No BMP4
+ BMP4
+ BMP4
washout
E
Ttr
Ttr expression relative to 18S rRNAs
Prdm16_OE
Prdm16_KO
No BMP4
+ BMP4
+ BMP4
washout

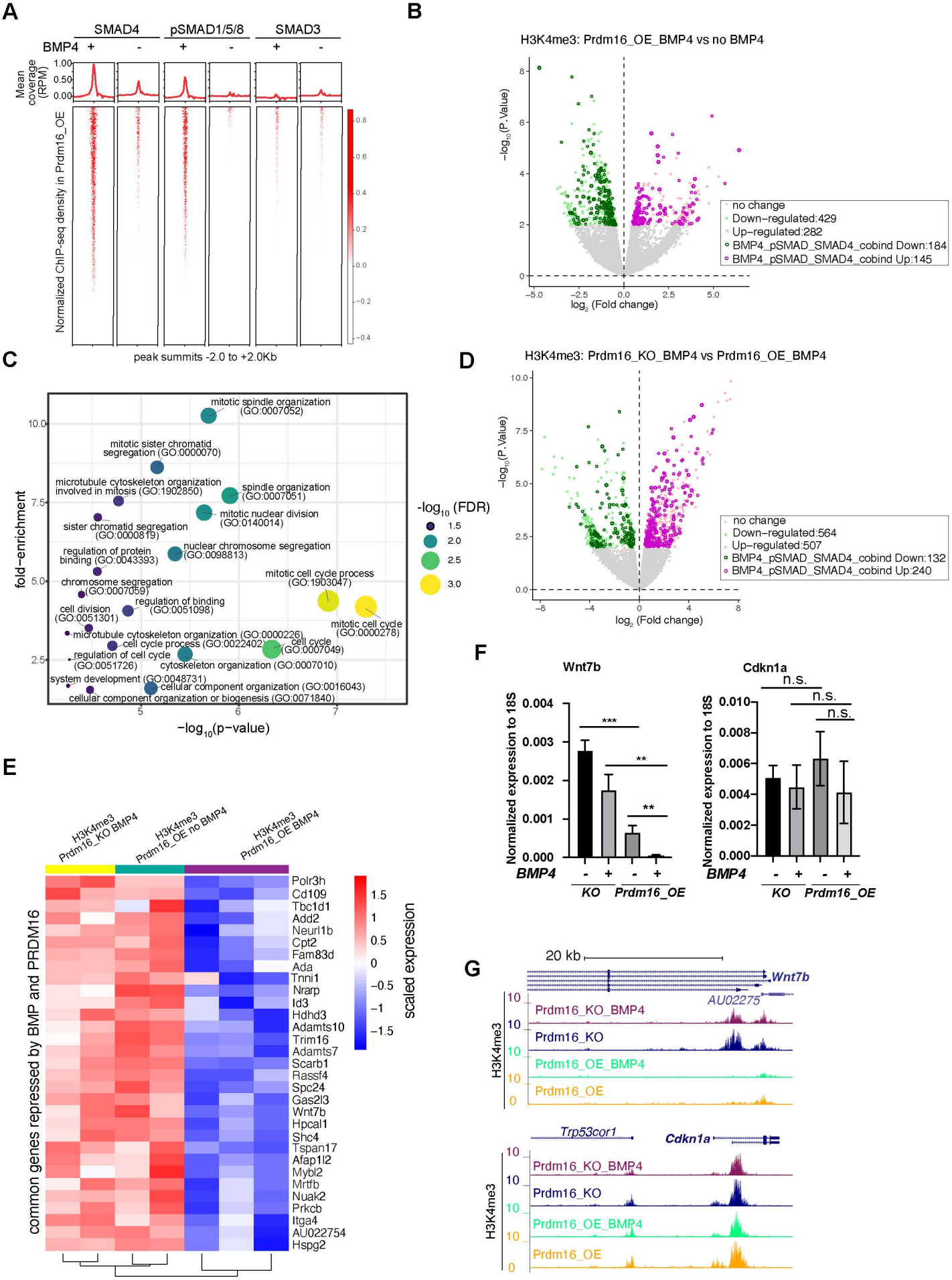
A
SMAD4
pSMAD1/5/8
SMAD3
BMP4 + - + - + -
Mean coverage (RPM)
Normalized ChIP-seq density in Prdm16_OE
peak summits -2.0 to +2.0Kb
B
H3K4me3: Prdm16_OE_BMP4 vs no BMP4
−log10(P.Value)
log2 (Fold change)
no change
Down−regulated:429
Up−regulated:282
BMP4_pSMAD_SMAD4_cobind Down:184
BMP4_pSMAD_SMAD4_cobind Up:145
C
fold−enrichment
−log10(p−value)
-log10 (FDR)
mitotic spindle organization (GO:0007052)
mitotic sister chromatid segregation (GO:0000070)
microtubule cytoskeleton organization involved in mitosis (GO:1902850)
spindle organization (GO:0007051)
mitotic nuclear division (GO:0140014)
sister chromatid segregation (GO:0000819)
regulation of protein binding (GO:0043393)
nuclear chromosome segregation (GO:0098813)
mitotic cell cycle process (GO:1903047)
chromosome segregation (GO:0007059)
regulation of binding (GO:0051098)
cell division (GO:0051301)
mitotic cell cycle (GO:0000278)
microtubule cytoskeleton organization (GO:0000226)
cell cycle process (GO:0022402)
cell cycle (GO:0007049)
regulation of cell cycle (GO:0051726)
cytoskeleton organization (GO:0007010)
system development (GO:0048731)
cellular component organization (GO:0016043)
cellular component organization or biogenesis (GO:0071840)
D
H3K4me3: Prdm16_KO_BMP4 vs Prdm16_OE_BMP4
−log10(P.Value)
log2 (Fold change)
no change
Down−regulated:564
Up−regulated:507
BMP4_pSMAD_SMAD4_cobind Down:132
BMP4_pSMAD_SMAD4_cobind Up:240
E
H3K4me3 Prdm16_KO BMP4
H3K4me3 Prdm16_OE no BMP4
H3K4me3 Prdm16_OE BMP4
common genes repressed by BMP and PRDM16
scaled expression
Polr3h
Cd109
Tbc1d1
Add2
Neurl1b
Cpt2
Fam83d
Ada
Tnni1
Nrarp
Id3
Hdhd3
Adamts10
Trim16
Adamts7
Scarb1
Rassf4
Spc24
Gas2l3
Wnt7b
Hpcal1
Shc4
Tspan17
Afap1l2
Mybl2
Mrtfb
Nuak2
Prkcb
Itga4
AU022754
Hspg2
F
Wnt7b
Cdkn1a
Normalized expression to 18S
n.s.
BMP4
KO
Prdm16_OE
G
20 kb
Wnt7b
AU02275
H3K4me3
Prdm16_KO_BMP4
Prdm16_KO
Prdm16_OE_BMP4
Prdm16_OE
Trp53cor1
Cdkn1a

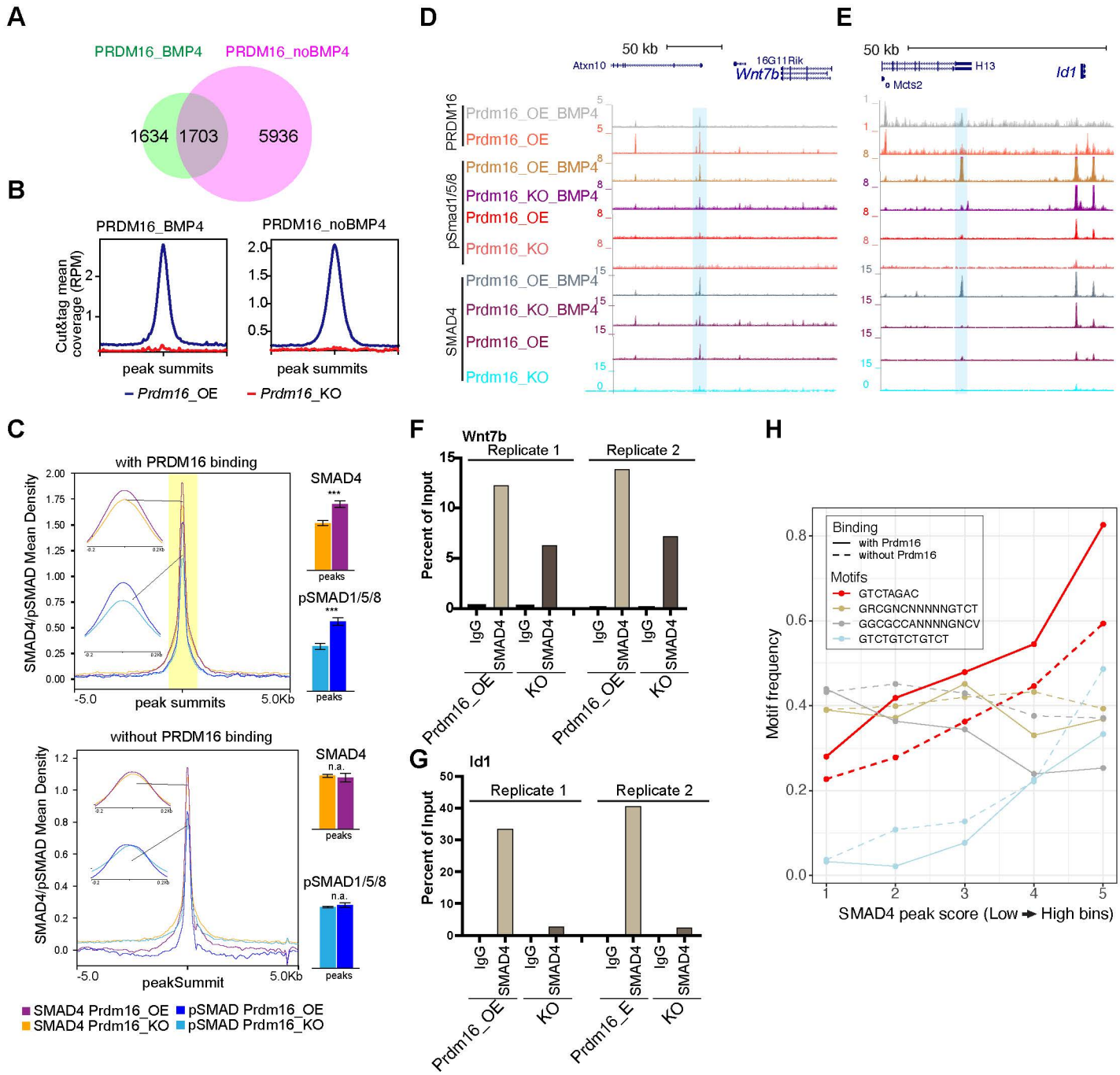
A
PRDM16_BMP4
PRDM16_noBMP4
1634
1703
5936
B
PRDM16_BMP4
PRDM16_noBMP4
Cut&tag mean coverage (RPM)
peak summits
Prdm16_OE
Prdm16_KO
C
with PRDM16 binding
SMAD4/pSMAD Mean Density
peak summits
SMAD4
pSMAD1/5/8
peaks
without PRDM16 binding
peakSummit
n.a.
SMAD4 Prdm16_OE
pSMAD Prdm16_OE
SMAD4 Prdm16_KO
pSMAD Prdm16_KO
D
50 kb
Atxn10
16G11Rik
Wnt7b
PRDM16
Prdm16_OE_BMP4
Prdm16_OE
pSmad1/5/8
Prdm16_KO_BMP4
Prdm16_KO
SMAD4
E
H13
Id1
Mcts2
F
Wnt7b
Replicate 1
Replicate 2
Percent of Input
IgG
SMAD4
Prdm16_OE
KO
G
Id1
Prdm16_E
H
Binding
with Prdm16
without Prdm16
Motifs
GTCTAGAC
GRCGNCNNNNNGTCT
GGCGCCANNNNGNCV
GTCTGTCTGTCT
Motif frequency
SMAD4 peak score (Low → High bins)

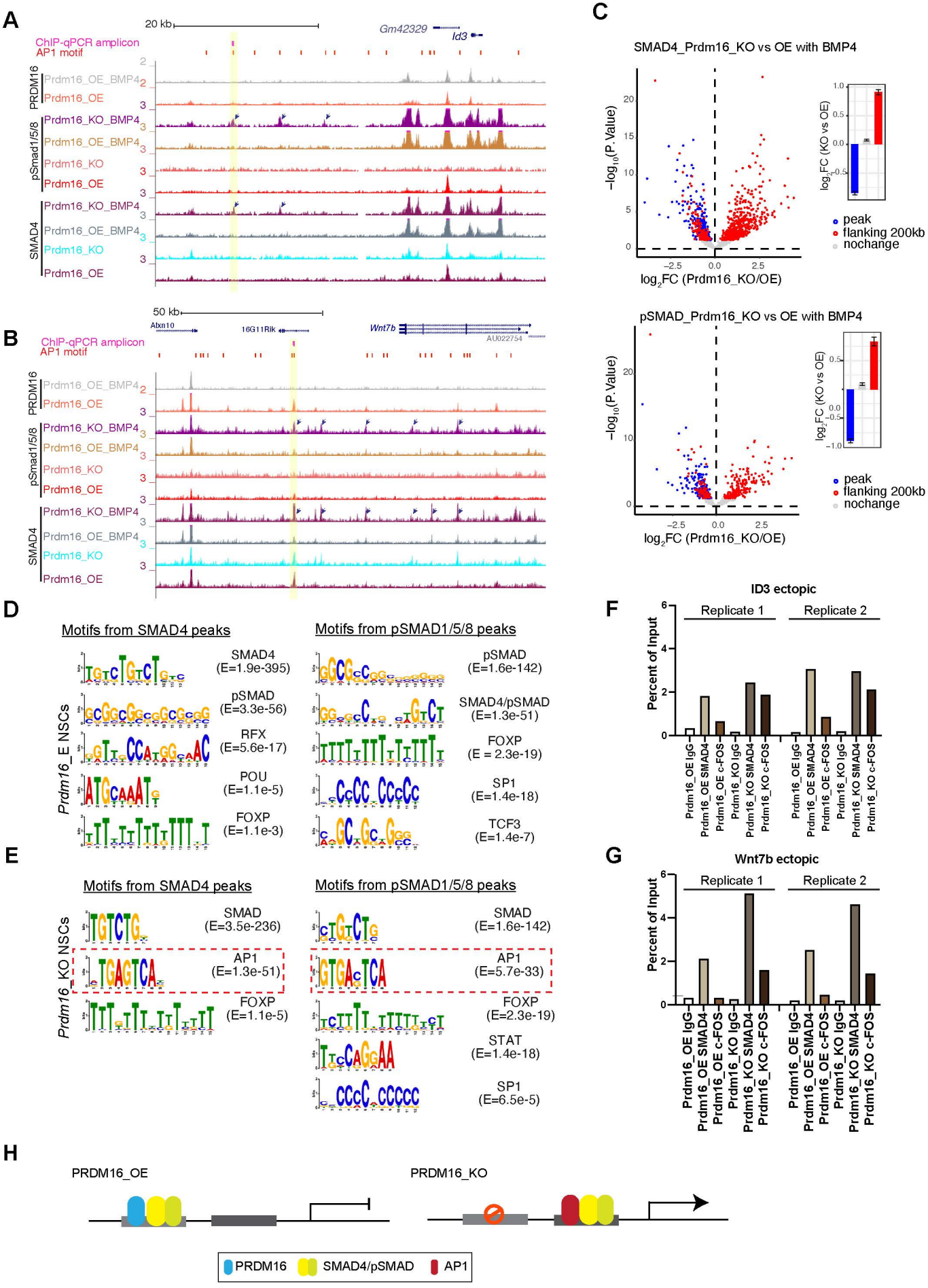
A
20 kb
Gm42329
Id3
ChIP-qPCR amplicon
AP1 motif
PRDM16
pSmad1/5/8
SMAD4
Prdm16_OE_BMP4
Prdm16_OE
Prdm16_KO_BMP4
Prdm16_KO
B
50 kb
Atxn10
16G11Rik
Wnt7b
AU022754
C
SMAD4_Prdm16_KO vs OE with BMP4
pSMAD_Prdm16_KO vs OE with BMP4
−log10(P.Value)
log2FC (Prdm16_KO/OE)
log2FC (KO vs OE)
peak
flanking 200kb
nochange
D
Motifs from SMAD4 peaks
Motifs from pSMAD1/5/8 peaks
Prdm16_E NSCs
SMAD4 (E=1.9e-395)
pSMAD (E=3.3e-56)
RFX (E=5.6e-17)
POU (E=1.1e-5)
FOXP (E=1.1e-3)
pSMAD (E=1.6e-142)
SMAD4/pSMAD (E=1.3e-51)
FOXP (E = 2.3e-19)
SP1 (E=1.4e-18)
TCF3 (E=1.4e-7)
E
Prdm16_KO NSCs
SMAD (E=3.5e-236)
AP1 (E=1.3e-51)
FOXP (E=1.1e-5)
SMAD (E=1.6e-142)
AP1 (E=5.7e-33)
FOXP (E=2.3e-19)
STAT (E=1.4e-18)
SP1 (E=6.5e-5)
F
ID3 ectopic
Replicate 1
Replicate 2
Percent of Input
Prdm16_OE IgG
Prdm16_OE SMAD4
Prdm16_OE c-FOS
Prdm16_KO IgG
Prdm16_KO SMAD4
Prdm16_KO c-FOS
G
Wnt7b ectopic
H
PRDM16_OE
PRDM16_KO
PRDM16
SMAD4/pSMAD
AP1

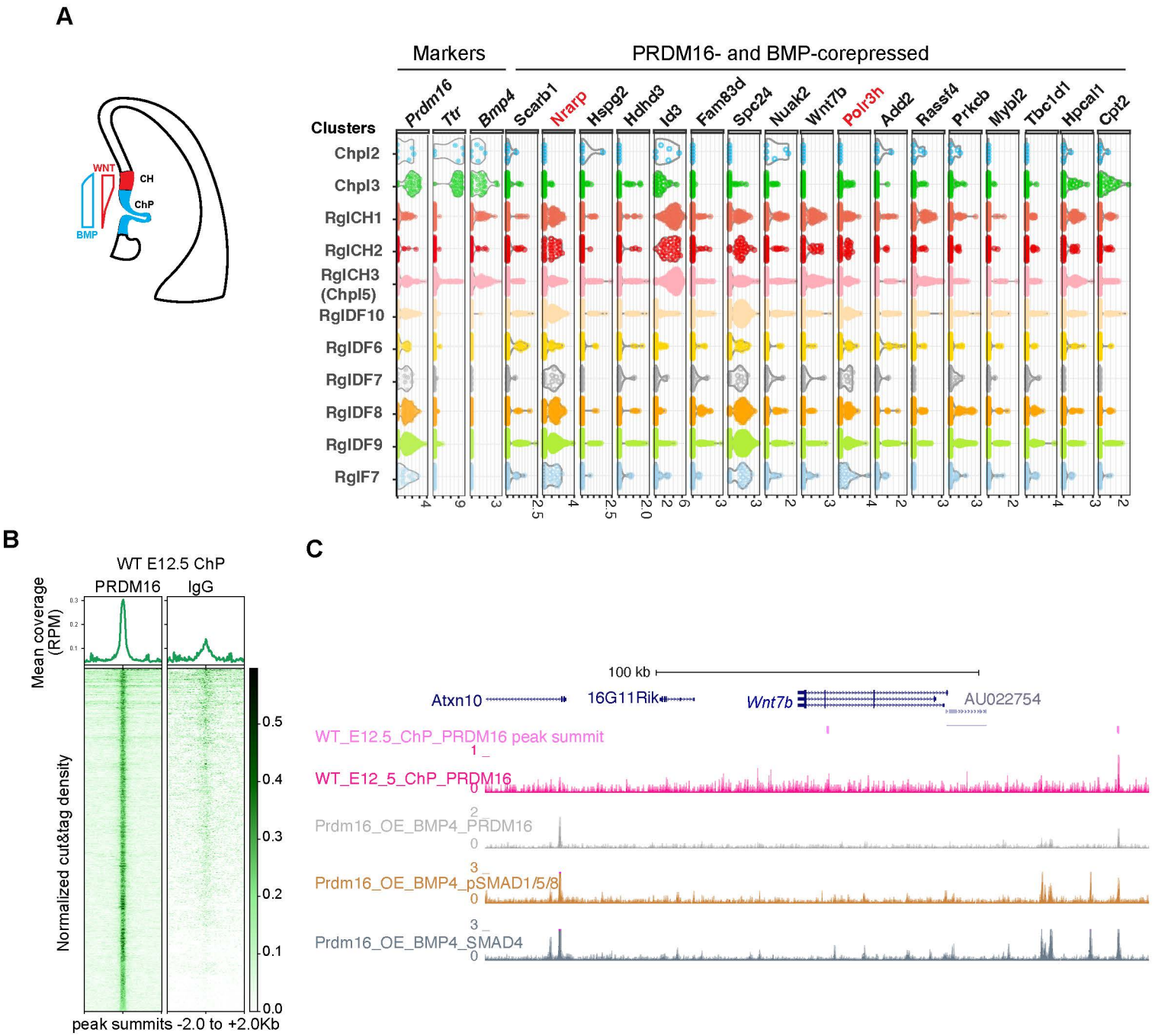
A
Markers
PRDM16- and BMP-corepressed
Clusters
Prdm16
Ttr
Bmp4
Scarb1
Nrarp
Hspg2
Hdhd3
Id3
Fam83d
Spc24
Nuak2
Wnt7b
Polr3h
Add2
Rassf4
Prkcb
Mybl2
Tbc1d1
Hpcal1
Cpt2
Chpl2
Chpl3
RglCH1
RglCH2
RglCH3 (Chpl5)
RglDF10
RglDF6
RglDF7
RglDF8
RglDF9
RglF7
WNT
CH
ChP
BMP
B
WT E12.5 ChP
PRDM16
IgG
Mean coverage (RPM)
Normalized cut&tag density
peak summits -2.0 to +2.0Kb
C
100 kb
Atxn10
16G11Rik
Wnt7b
AU022754
WT_E12.5_ChP_PRDM16 peak summit
WT_E12_5_ChP_PRDM16
Prdm16_OE_BMP4_PRDM16
Prdm16_OE_BMP4_pSMAD1/5/8
Prdm16_OE_BMP4_SMAD4

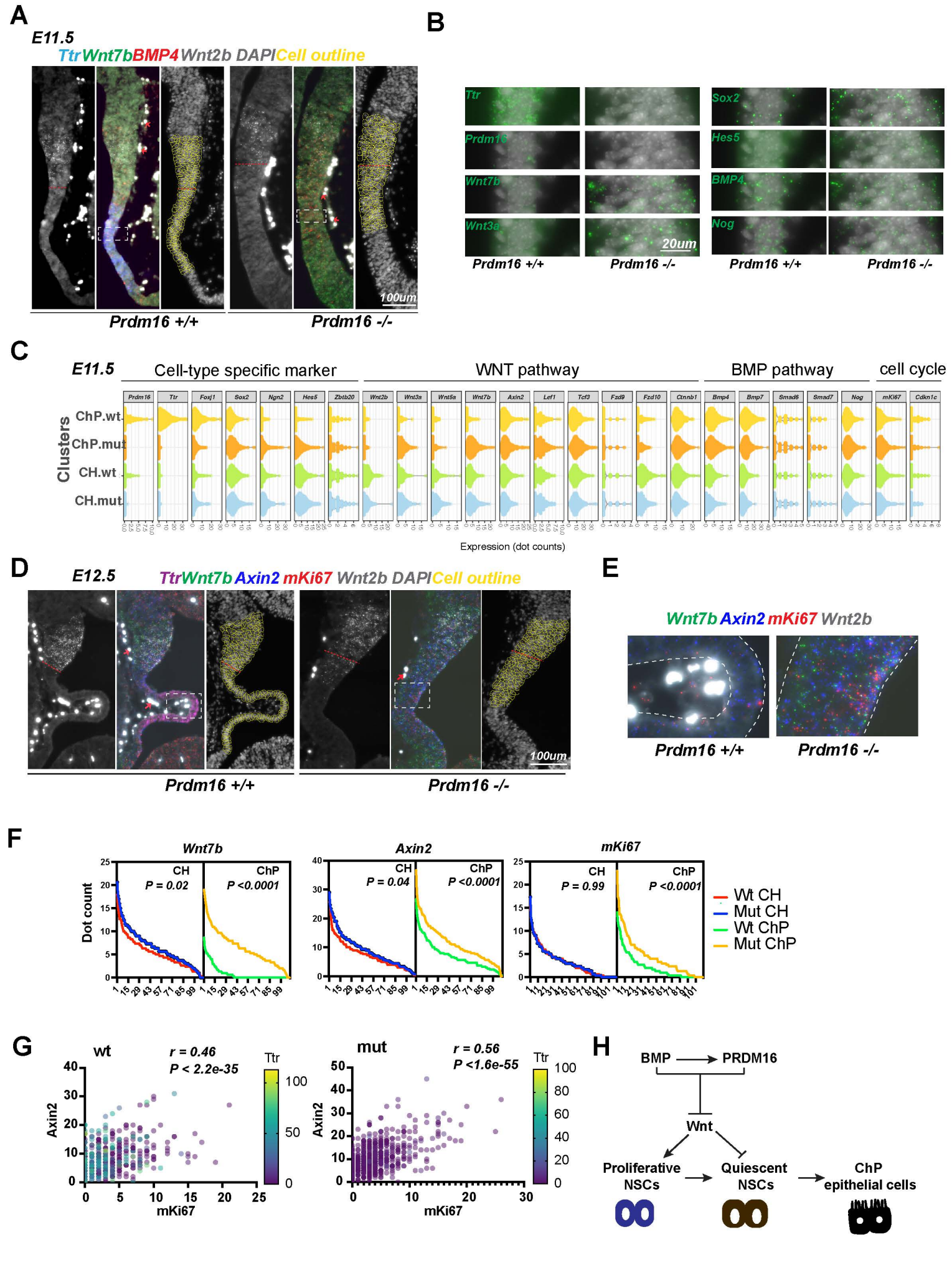
A
E11.5
Ttr Wnt7b BMP4 Wnt2b DAPI Cell outline
100um
Prdm16 +/+
Prdm16 -/-
B
Ttr
Prdm16
Wnt7b
Wnt3a
Sox2
Hes5
BMP4
Nog
20um
Prdm16 +/+
Prdm16 -/-
Prdm16 +/+
Prdm16 -/-
C
E11.5
Cell-type specific marker
WNT pathway
BMP pathway
cell cycle
Prdm16 Ttr Foxj1 Sox2 Ngn2 Hes5 Zbtb20 Wnt2b Wnt3a Wnt5a Wnt7b Axin2 Lef1 Tcf3 Fzd9 Fzd10 Ctnnb1 Bmp4 Bmp7 Smad6 Smad7 Nog mKi67 Cdkn1c
Clusters
ChP.wt
ChP.mut
CH.wt
CH.mut
Expression (dot counts)
D
E12.5
Ttr Wnt7b Axin2 mKi67 Wnt2b DAPI Cell outline
100um
Prdm16 +/+
Prdm16 -/-
E
Wnt7b Axin2 mKi67 Wnt2b
Prdm16 +/+
Prdm16 -/-
F
Wnt7b
Axin2
mKi67
Dot count
CH
P = 0.02
ChP
P <0.0001
CH
P = 0.04
ChP
P <0.0001
CH
P = 0.99
ChP
P <0.0001
Wt CH
Mut CH
Wt ChP
Mut ChP
G
wt
r = 0.46
P < 2.2e-35
Ttr
Axin2
mKi67
mut
r = 0.56
P <1.6e-55
Ttr
Axin2
mKi67
H
BMP
PRDM16
Wnt
Proliferative NSCs
Quiescent NSCs
ChP epithelial cells

Supplementary Figure 1. *Prdm16* depletion affects ChP epithelial specification without altering dorsal midline patterning

(**A**) Immunostaining of PRDM16 and SOX2 on E10.5 control and homozygous brain sections. ChP regions are outlined in white. (**B**) RNA in situ hybridization for *Ttr* in E12.5 control and Prdm16 null mutant hindbrains. (**C**) RNA in situ hybridization using *Wnt2b* and *Bmp4* probes on control and mutant forebrains at E11.5 and E12.5. (**D**) SOX2 immunostaining on E12.5 brain sections. ChP areas are marked with brackets. Relative SOX2 signal intensity between ChP and neurogenic regions is quantified. Error bars represent standard deviation (SD), n = 3. Statistical analysis by unpaired t-test (***P < 0.001; **P < 0.01; *P < 0.05; n.s., not significant).

Supplementary Figure 2. NSC culture assay reveals PRDM16 function in NSCs.

(**A**) Immunostaining for PRDM16 and FLAG with DAPI in NSCs expressing *Flag_Prdm16*, wild-type (WT) NSCs, and *Prdm16_KO* NSCs. PRDM16 is sparsely expressed and cytoplasmic in WT NSCs, whereas FLAG_PRDM16 is robustly expressed in both cytoplasm and nucleus. (**B**) RT-qPCR measurement of *Prdm16* mRNA levels normalized to the 18S rRNAs in the indicated genotypes and conditions, from three biological replicates, each with two technical replicates. Statistical significance was calculated using unpaired t-test (***, p<0.001; **, p< 0.01; *, p<0.05; n.s., non-significant). (**C**) Immunostaining of dissociated NSCs on Matrigel for mKI67, EdU and Sox2. WT_CDH denotes WT NSCs infected with the pCDH vector. (**D-F**). Quantification of marker-positive cell fractions under three culture conditions. KO_CDH indicates *Prdm16_KO* NSCs infected with the pCDH vector. (**G**) RT-qPCR measurement of *Ttr* mRNA levels normalized to 18S rRNAs, from three biological replicates**.** (**H**) Immunostaining for SMAD4, pSMAD1/5/8 and FLAG together with DAPI in NSCs. Nuclear localization of SMAD4 and pSMAD1/5/8 are enhanced following BMP4 treatment.

Supplementary Figure 3. Overlapping analysis of SMAD4, pSMAD1/5/8 and SMAD3 CUT&TAG peaks.

(**A**) Venn diagrams showing overlapping SMAD4, pSMAD1/5/8 and SMAD3 ChIP-seq peaks in *Prdm16_OE* NSCs with or without BMP4. (**B-C**) Overlap Venn diagrams and bar plots for SMAD4, pSMAD1/5/8 and SMAD3 ChIP-seq peaks in *Prdm16_OE* NSCs with BMP4 (B) and

without BMP4 (C). (**D**) Genome browser tracks of the *Prdm16* locus showing increased SMAD4 and pSMAD1/5/8 binding at the two highlighted enhancer regions. (**E**) Genome browser tracks showing the H3K4me4 CUT&TAG signals at the indicated loci. **(F-G, I-K**). RT-qPCR measurement of the indicated genes normalized to 18S rRNAs, from three biological replicates**.** Error bars represent standard deviation (SD). (**H**) Schematic of the NDC80 complex. Statistical significance is calculated using unpaired t-test. ***, p<0.001; **, p< 001; *, p<0.05; n.s., non-significant.

Supplementary Figure 4. PRDM16 assists SMAD4/pSMAD1/5/8 genomic binding to their co-bound sites.

(**A-C**) Venn diagrams and interaction plots showing overlap between PRDM16 CUT&TAG peaks in *Prdm16_OE* cells with BMP4, SMAD4 (A), pSMAD1/5/8 (B), SMAD3 (C) ChIP-seq peaks in *Prdm16_OE* and *Prdm16_KO* cells with BMP4. (**D**) Sequential ChIP-qPCR using IgG or PRDM16 antibodies followed by SMAD4 antibody. The *Ins* gene serves as a negative control. (**E**) Frequency of each DNA motif in SMAD4/pSMAD1/5/8 ChIP-seq peaks with or without PRDM16 co-binding in BMP4 treated *Prdm16_OE* cells.

Supplementary Figure 5. Wnt genes are potential targets regulated by PRDM16.

(A) Violin plots of scRNA-seq expression at E12.5 for the indicated genes in cell type clusters (reanalyzed from La Manno et al., 2021 as in Figure 6A). Genes shown here have lower expression than those in main Figure 6A. Red text indicates genes without PRDM16 binding in E12.5 ChP. (**B**) Intersection plot of PRDM16 CUT&Tag peaks across three biological replicates; commonly shared peaks are highlighted. (**C**) Bar graph showing proportion of genes with PRDM16 binding in E12.5 ChP. (**D**) Genome browser view of Wnt3a locus showing PRDM16 CUT&Tag and SMAD ChIP-seq tracks. (**E**) Violin plots of gene expression across reanalyzed cell type clusters.

Supplementary Figure 6. Altered expression of Wnt pathway and proliferation genes in *Prdm16* mutant ChP cells

(**A**) Violin plots showing expression changes of 24 examined genes (including ChP, neural, BMP pathway, Wnt pathway genes and *mKi67*) across 110 CH and 110 ChP cells per sample (330 cells per genotype, 3 WT and mutant pairs). (**B**) SCRINSHOT images showing *Wnt3a* mRNA in WT

and *Prdm16* mutant brains. (**C**) Dot quantification of *Wnt3a* expression in CH and ChP regions across three replicates. X-axis: cell ID; Y-axis: average dot count. *P* value was calculated using area under the ROC curve in Prism Graphpad. (**D**) Heatmap of gene expression correlations. In WT cells, BMP genes cluster with *Ttr* and *Foxj1*, while Wnt genes cluster with *mKi67*. In mutants, BMP genes correlation with ChP markers is reduced, while Wnt-*mKi67* correlations is maintained.

Supplementary Figure 7. Expression of BMP and Wnt genes in the developing 4th ventricle ChP.

(**A-B**) SCRINSHOT images showing mRNA levels of ChP marker and BMP genes (A), and Wnt genes and *mKi67* (**B**), in wild-type and *Prdm16* mutant brains. Green: mRNA signals; grey: DAPI. (**C**) Enlarged view of SCRINSHOT images. Note the increased dot count for Wnt genes and *mKi67* in the mutant.

Supplementary Figure 8. Increased expression of additional PRDM16 target genes in *Prdm16* mutant ChP.

(**A**) Full images of SCRINSHOT signals for genes shown in Figure 7B. (**B**) Example of image segmentation for SCRINSHOT dot quantification.

Supplementary Figure 9. Increased expression of additional PRDM16 target genes in *Prdm16* mutant ChP.

(**A**) SCRINSHOT images showing mRNA levels of indicated genes in wild-type and *Prdm16* mutant brains; enlarged views at right. Gene expression is elevated in mutants. (**B**) Quantification of dot counts in CH and ChP regions (110 cells each) across three replicates. *Prdm16* and *Wnt2b* are included as controls. Error bars denote SD. Statistical analysis via paired t-test (***$P < 0.001$; **$P < 0.01$; *$P < 0.05$; n.s., not significant).

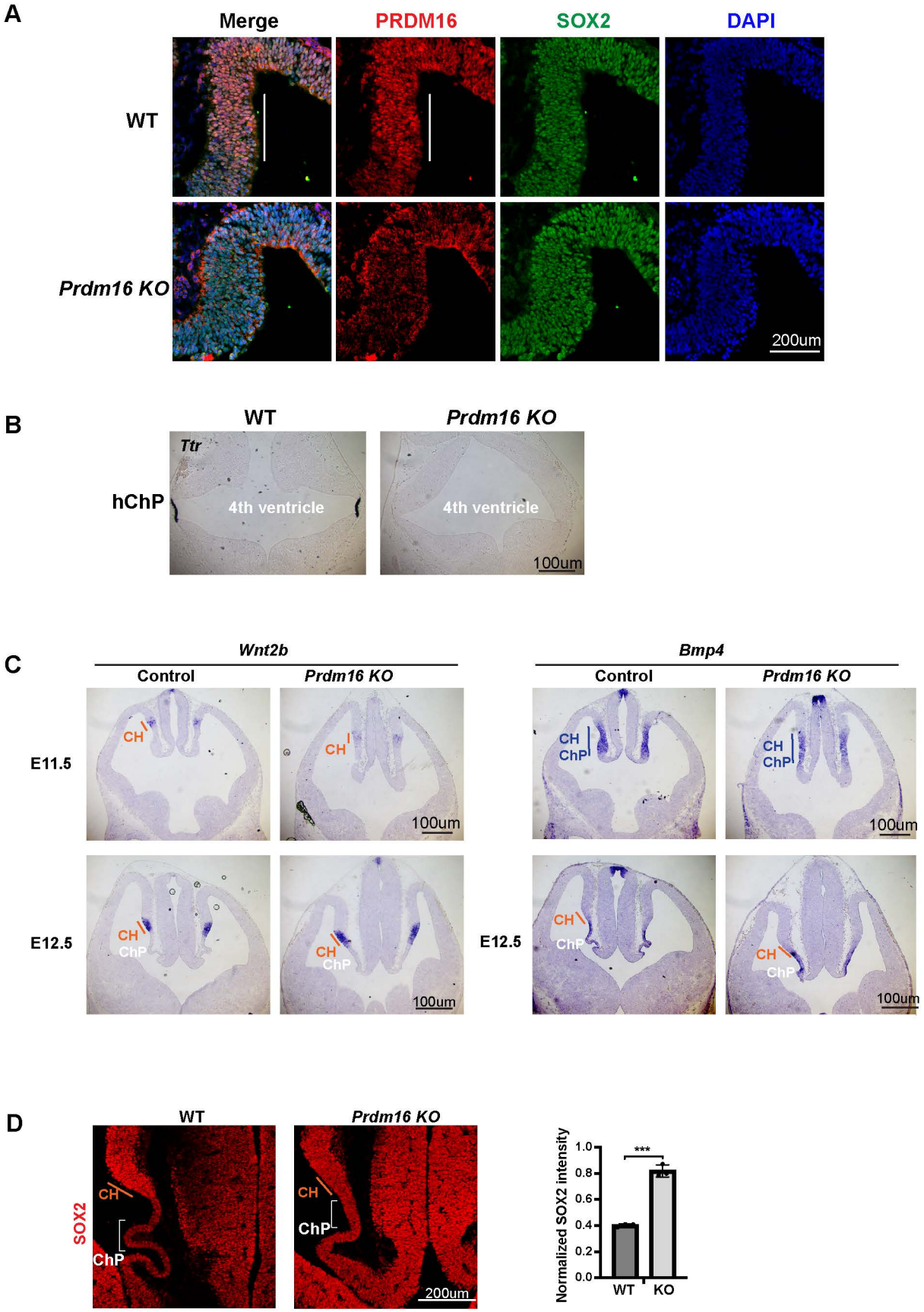
A
Merge
PRDM16
SOX2
DAPI
WT
Prdm16 KO
200um
B
WT
Prdm16 KO
hChP
Ttr
4th ventricle
4th ventricle
100um
C
Wnt2b
Control
Prdm16 KO
Bmp4
Control
Prdm16 KO
E11.5
E12.5
E12.5
CH
ChP
100um
D
WT
Prdm16 KO
SOX2
CH
ChP
200um
Normalized SOX2 intensity
1.0
0.8
0.6
0.4
0.2
0.0
***
WT
KO

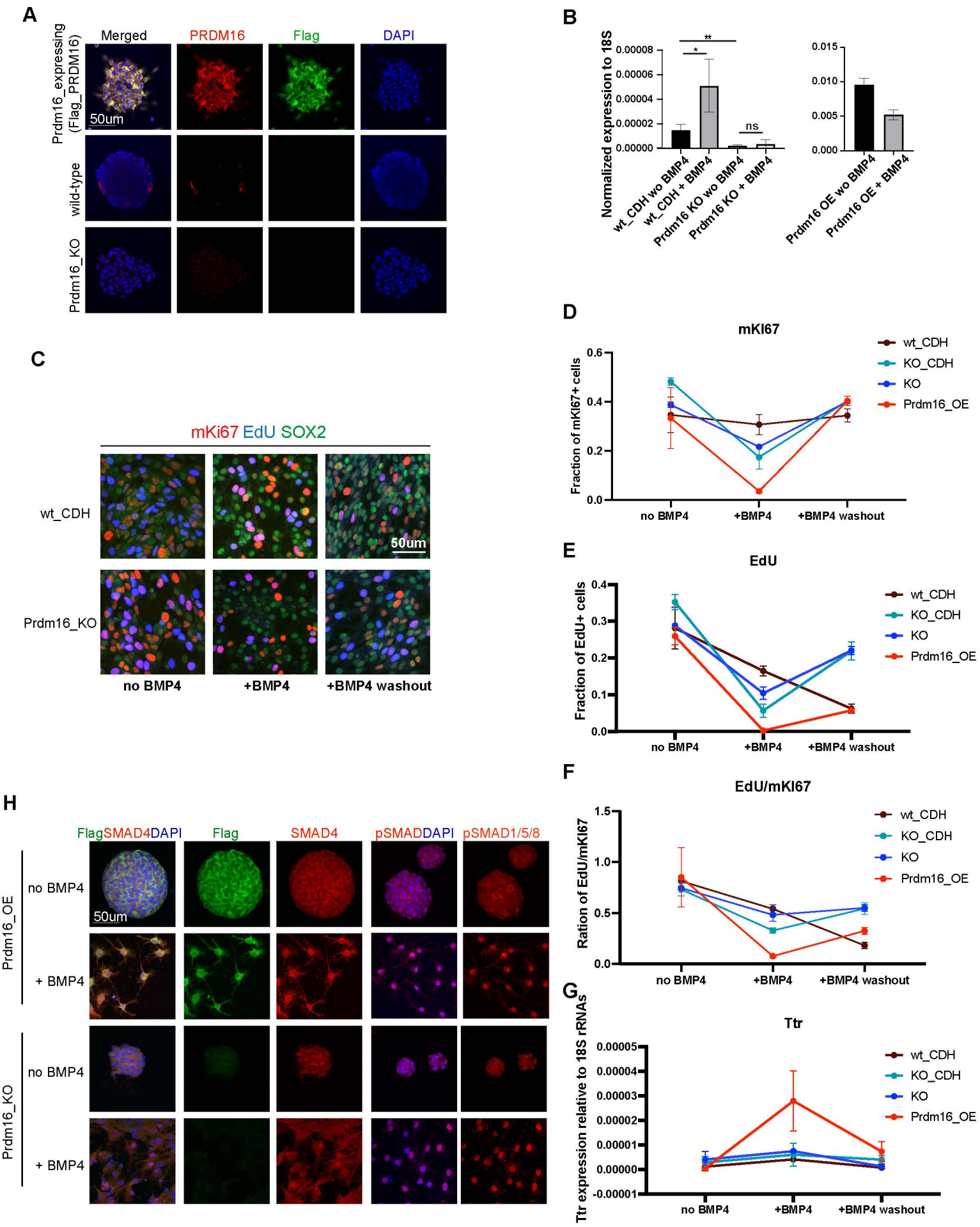
A
Merged
PRDM16
Flag
DAPI
Prdm16_expressing (Flag_PRDM16)
wild-type
Prdm16_KO
50um
B
Normalized expression to 18S
0.00008
0.00006
0.00004
0.00002
0.00000
**
*
ns
wt_CDH wo BMP4
wt_CDH + BMP4
Prdm16 KO wo BMP4
Prdm16 KO + BMP4
0.015
0.010
0.005
0.000
Prdm16 OE wo BMP4
Prdm16 OE + BMP4
C
mKi67 EdU SOX2
wt_CDH
Prdm16_KO
50um
no BMP4
+BMP4
+BMP4 washout
D
mKI67
Fraction of mKI67+ cells
0.6
0.4
0.2
0.0
wt_CDH
KO_CDH
KO
Prdm16_OE
no BMP4
+BMP4
+BMP4 washout
E
EdU
Fraction of EdU+ cells
0.4
0.3
0.2
0.1
0.0
wt_CDH
KO_CDH
KO
Prdm16_OE
no BMP4
+BMP4
+BMP4 washout
F
EdU/mKI67
Ration of EdU/mKI67
1.5
1.0
0.5
0.0
wt_CDH
KO_CDH
KO
Prdm16_OE
no BMP4
+BMP4
+BMP4 washout
G
Ttr
Ttr expression relative to 18S rRNAs
0.00005
0.00004
0.00003
0.00002
0.00001
0.00000
-0.00001
wt_CDH
KO_CDH
KO
Prdm16_OE
no BMP4
+BMP4
+BMP4 washout
H
FlagSMAD4DAPI
Flag
SMAD4
pSMADDAPI
pSMAD1/5/8
Prdm16_OE
no BMP4
+ BMP4
Prdm16_KO
no BMP4
+ BMP4
50um

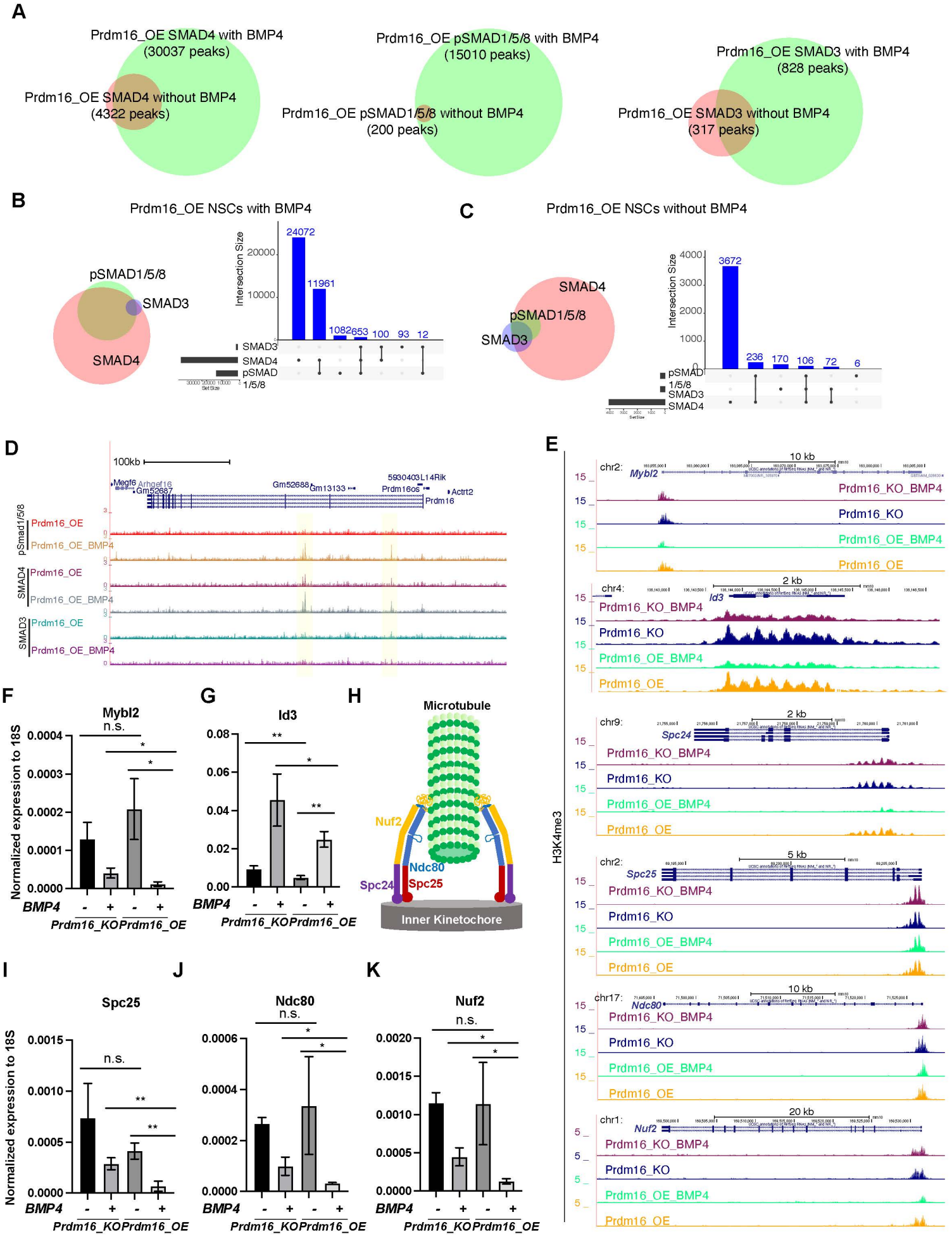
A
Prdm16_OE SMAD4 with BMP4
(30037 peaks)
Prdm16_OE SMAD4 without BMP4
(4322 peaks)
Prdm16_OE pSMAD1/5/8 with BMP4
(15010 peaks)
Prdm16_OE pSMAD1/5/8 without BMP4
(200 peaks)
Prdm16_OE SMAD3 with BMP4
(828 peaks)
Prdm16_OE SMAD3 without BMP4
(317 peaks)
B
Prdm16_OE NSCs with BMP4
pSMAD1/5/8
SMAD3
SMAD4
Intersection Size
24072
11961
1082
653
100
93
12
Set Size
C
Prdm16_OE NSCs without BMP4
SMAD4
pSMAD1/5/8
SMAD3
3672
236
170
106
72
6
D
100kb
Megf6
Arhgef16
Gm52687
Gm52688
Gm13133
5930403L14Rik
Prdm16os
Actrt2
Prdm16
pSmad1/5/8
Prdm16_OE
Prdm16_OE_BMP4
SMAD4
SMAD3
E
10 kb
chr2:
Mybl2
Prdm16_KO_BMP4
Prdm16_KO
Prdm16_OE_BMP4
Prdm16_OE
2 kb
chr4:
Id3
2 kb
chr9:
Spc24
5 kb
chr2:
Spc25
10 kb
chr17:
Ndc80
20 kb
chr1:
Nuf2
H3K4me3
F
Mybl2
n.s.
Normalized expression to 18S
BMP4
Prdm16_KO
Prdm16_OE
G
Id3
H
Microtubule
Nuf2
Ndc80
Spc24
Spc25
Inner Kinetochore
I
Spc25
n.s.
J
Ndc80
n.s.
K
Nuf2
n.s.

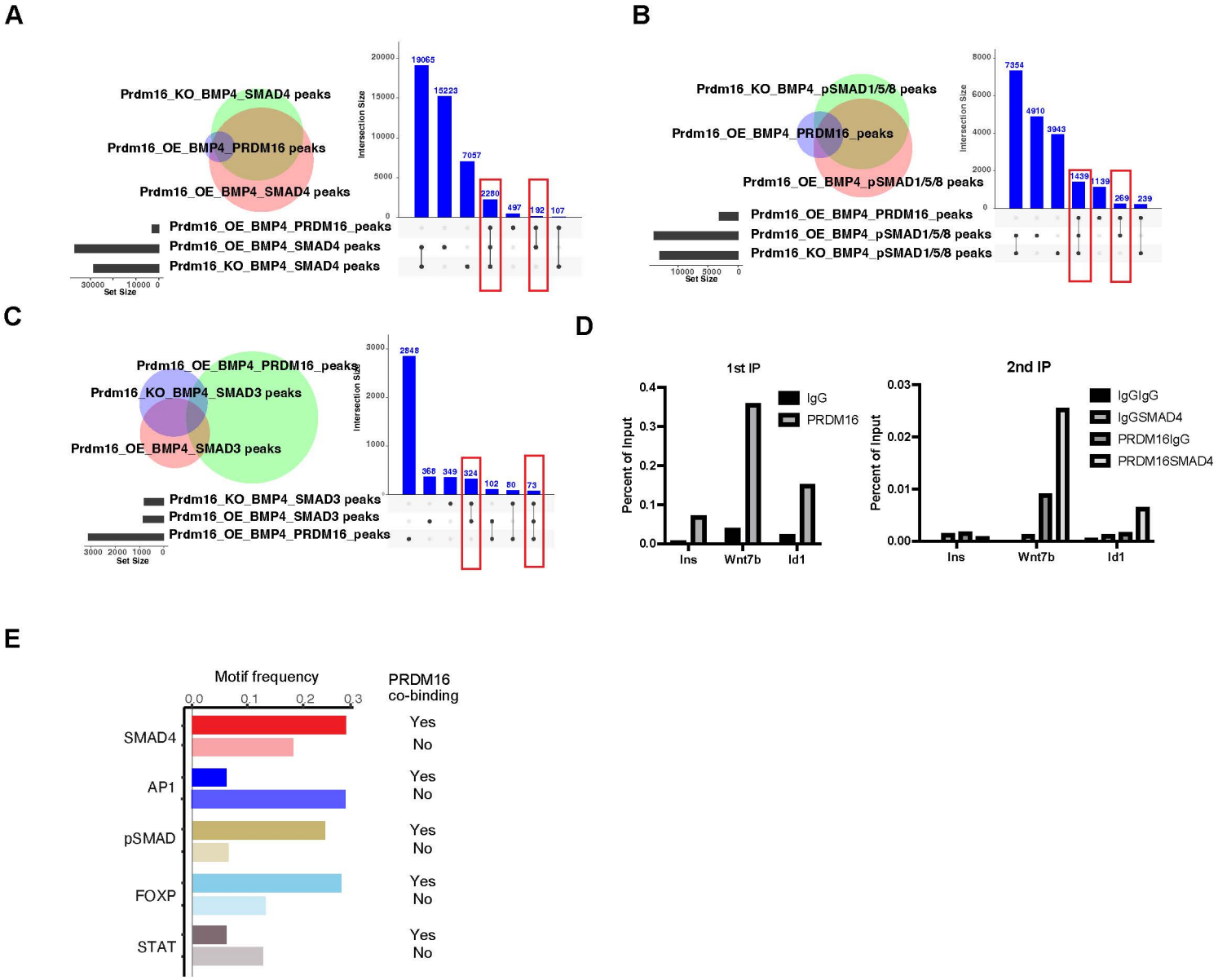
A
Prdm16_KO_BMP4_SMAD4 peaks
Prdm16_OE_BMP4_PRDM16 peaks
Prdm16_OE_BMP4_SMAD4 peaks
Prdm16_OE_BMP4_PRDM16_peaks
Prdm16_OE_BMP4_SMAD4 peaks
Prdm16_KO_BMP4_SMAD4 peaks
Intersection Size
Set Size
19065
15223
7057
2280
497
192
107
B
Prdm16_KO_BMP4_pSMAD1/5/8 peaks
Prdm16_OE_BMP4_PRDM16_peaks
Prdm16_OE_BMP4_pSMAD1/5/8 peaks
Prdm16_OE_BMP4_PRDM16_peaks
Prdm16_OE_BMP4_pSMAD1/5/8 peaks
Prdm16_KO_BMP4_pSMAD1/5/8 peaks
Intersection Size
Set Size
7354
4910
3943
1439
1139
269
239
C
Prdm16_OE_BMP4_PRDM16_peaks
Prdm16_KO_BMP4_SMAD3 peaks
Prdm16_OE_BMP4_SMAD3 peaks
Prdm16_KO_BMP4_SMAD3 peaks
Prdm16_OE_BMP4_SMAD3 peaks
Prdm16_OE_BMP4_PRDM16_peaks
Intersection Size
Set Size
2848
368
349
324
102
80
73
D
1st IP
IgG
PRDM16
Percent of Input
Ins
Wnt7b
Id1
2nd IP
IgGIgG
IgGSMAD4
PRDM16IgG
PRDM16SMAD4
Percent of Input
Ins
Wnt7b
Id1
E
Motif frequency
PRDM16 co-binding
SMAD4
AP1
pSMAD
FOXP
STAT
Yes
No

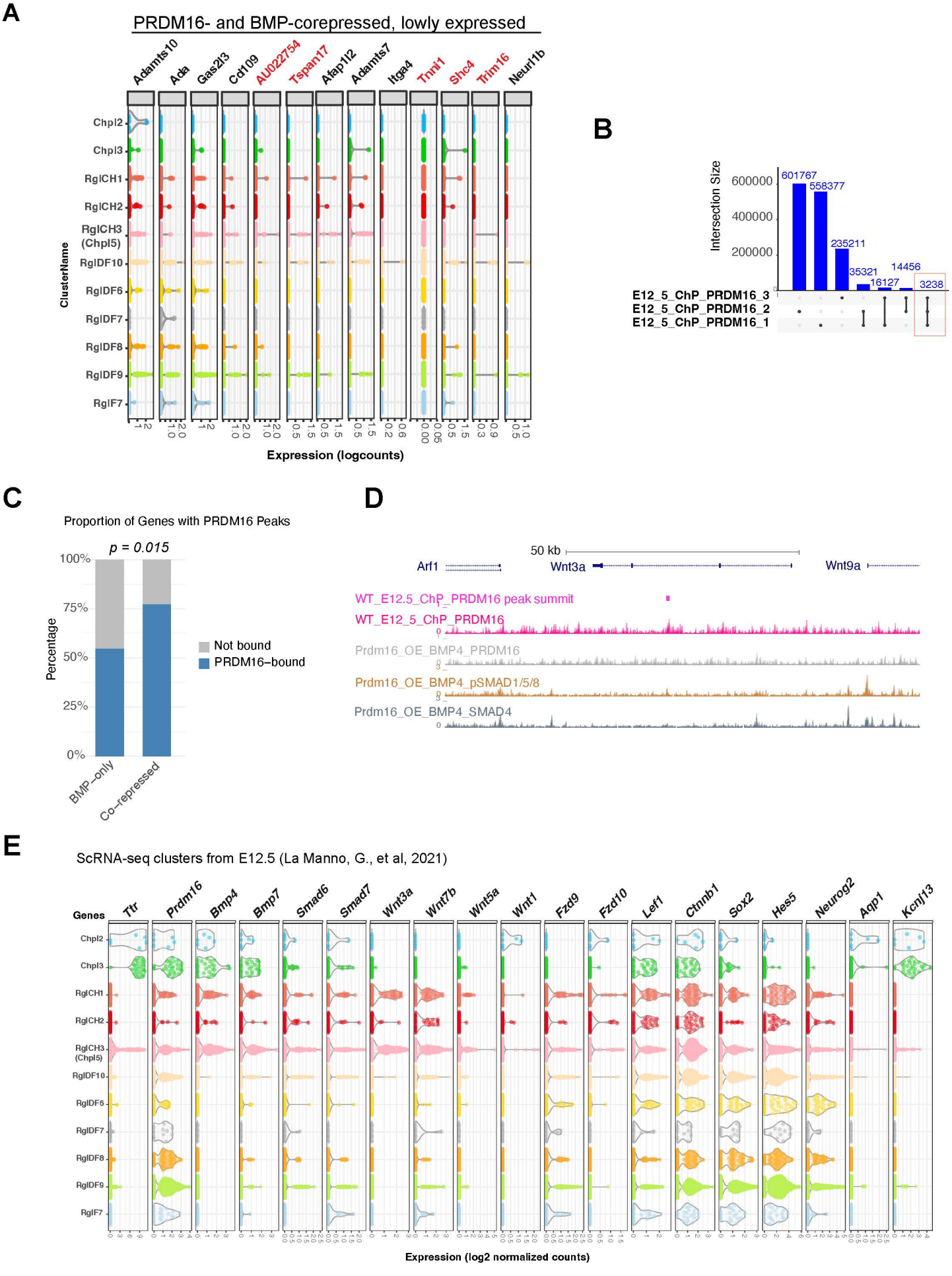
A
PRDM16- and BMP-corepressed, lowly expressed
Adamts10
Ada
Gas2l3
Cd109
AU022754
Tspan17
Afap1l2
Adamts7
Itga4
Tnni1
Shc4
Trim16
Neurl1b
ClusterName
Chpl2
Chpl3
RglCH1
RglCH2
RglCH3 (Chpl5)
RglDF10
RglDF6
RglDF7
RglDF8
RglDF9
RglF7
Expression (logcounts)
B
Intersection Size
601767
558377
235211
35321
16127
14456
3238
E12_5_ChP_PRDM16_3
E12_5_ChP_PRDM16_2
E12_5_ChP_PRDM16_1
C
Proportion of Genes with PRDM16 Peaks
p = 0.015
Percentage
Not bound
PRDM16–bound
BMP–only
Co–repressed
D
50 kb
Arf1
Wnt3a
Wnt9a
WT_E12.5_ChP_PRDM16 peak summit
WT_E12_5_ChP_PRDM16
Prdm16_OE_BMP4_PRDM16
Prdm16_OE_BMP4_pSMAD1/5/8
Prdm16_OE_BMP4_SMAD4
E
ScRNA-seq clusters from E12.5 (La Manno, G., et al, 2021)
Genes
Ttr
Prdm16
Bmp4
Bmp7
Smad6
Smad7
Wnt3a
Wnt7b
Wnt5a
Wnt1
Fzd9
Fzd10
Lef1
Ctnnb1
Sox2
Hes5
Neurog2
Aqp1
Kcnj13
Expression (log2 normalized counts)

A

E12.5

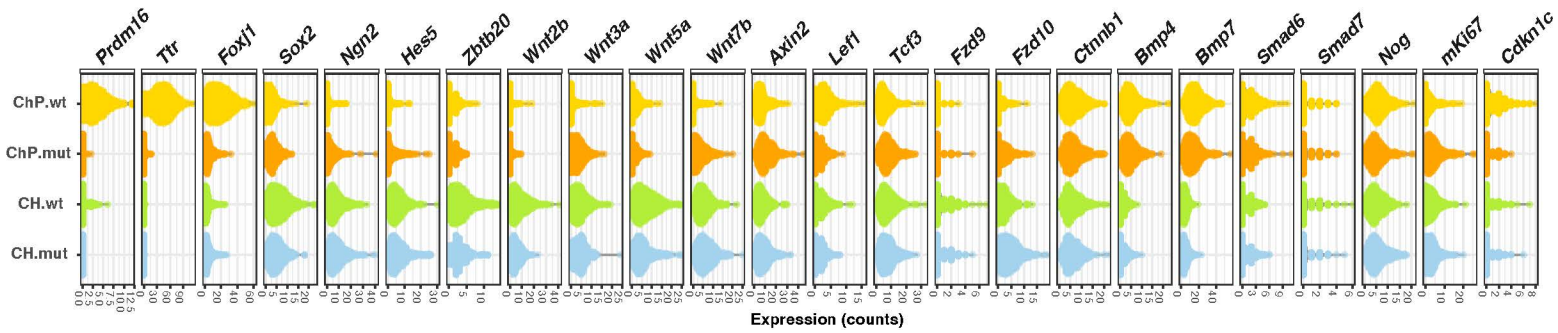

B

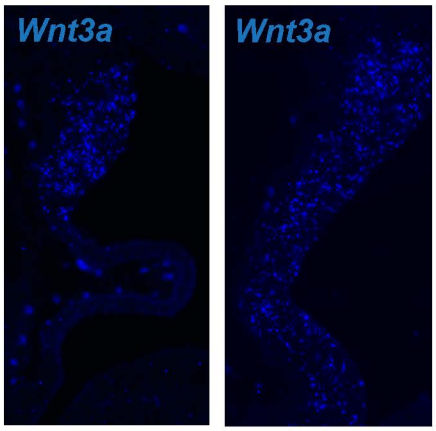

Prdm16 +/+ *Prdm16 -/-*

C

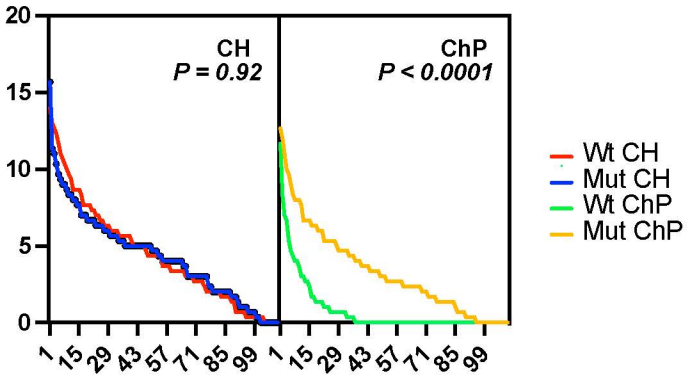

D

E12.5

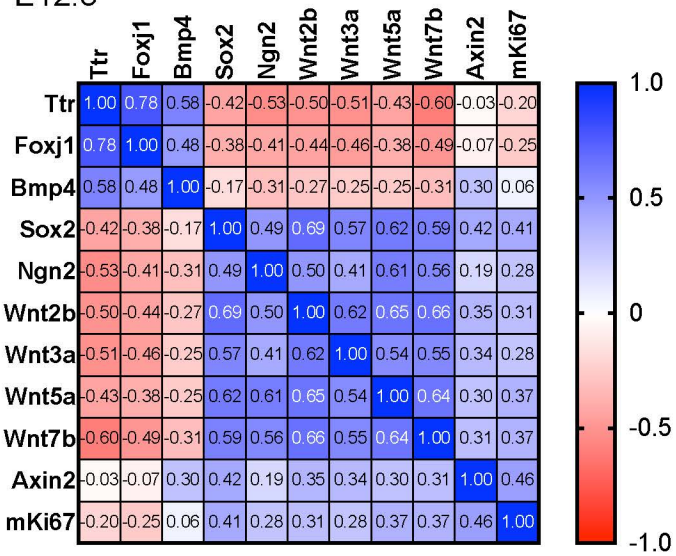

Prdm16 +/+

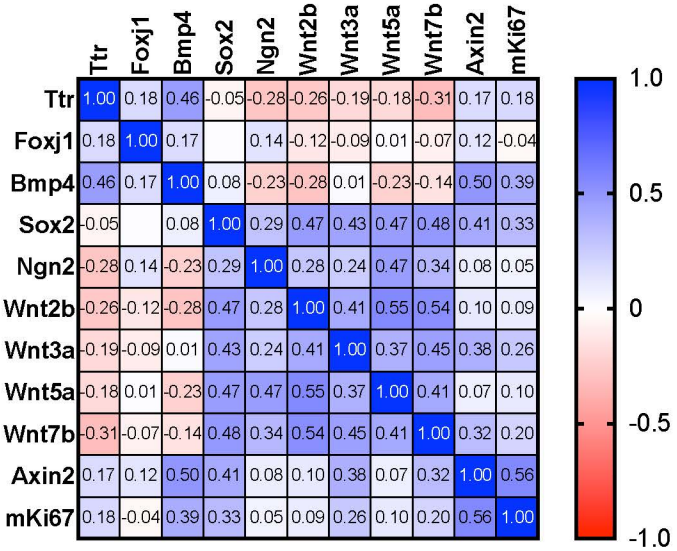

Prdm16 -/-

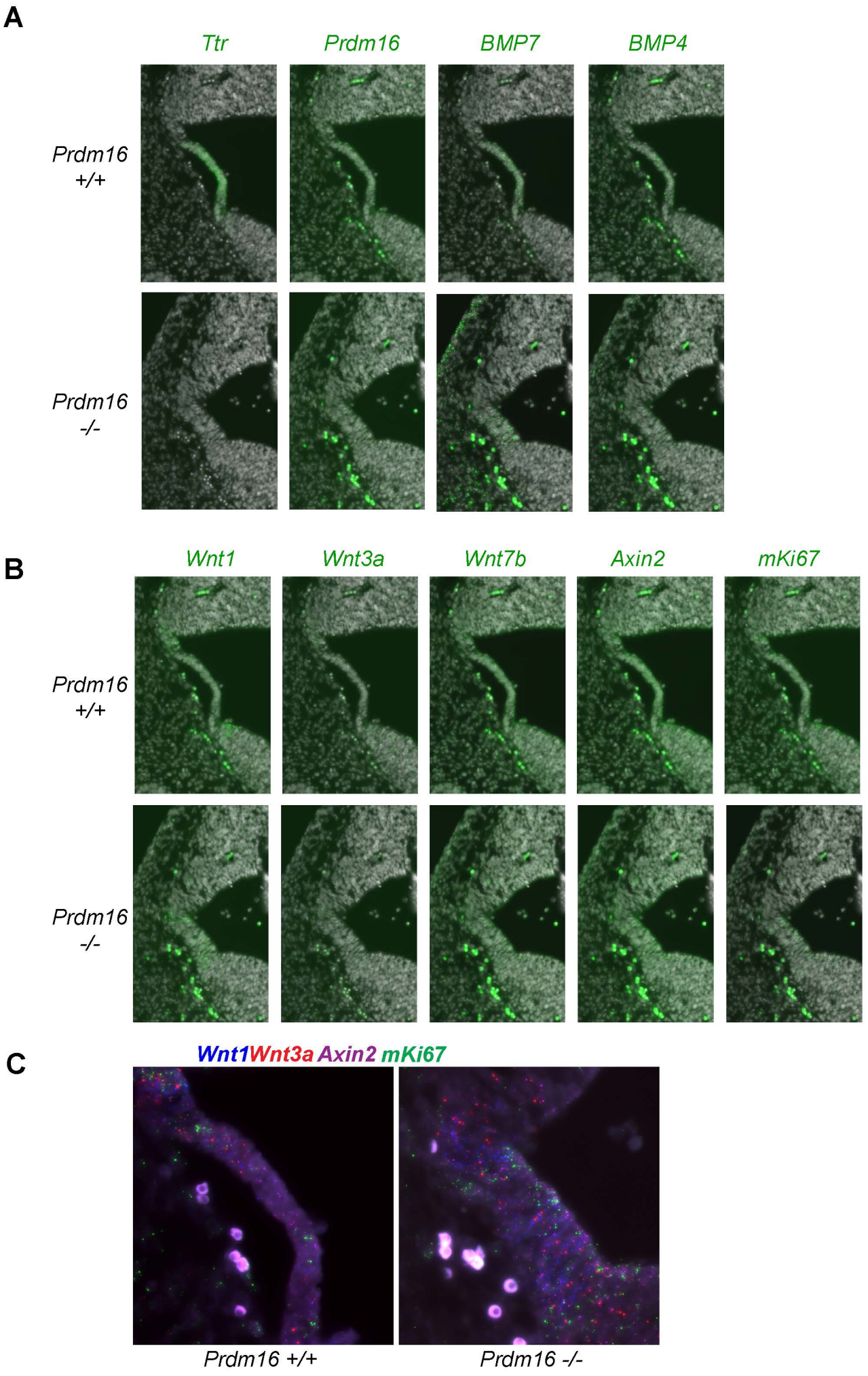
A
Ttr
Prdm16
BMP7
BMP4
Prdm16 +/+
Prdm16 -/-
B
Wnt1
Wnt3a
Wnt7b
Axin2
mKi67
Prdm16 +/+
Prdm16 -/-
C
Wnt1Wnt3a Axin2 mKi67
Prdm16 +/+
Prdm16 -/-

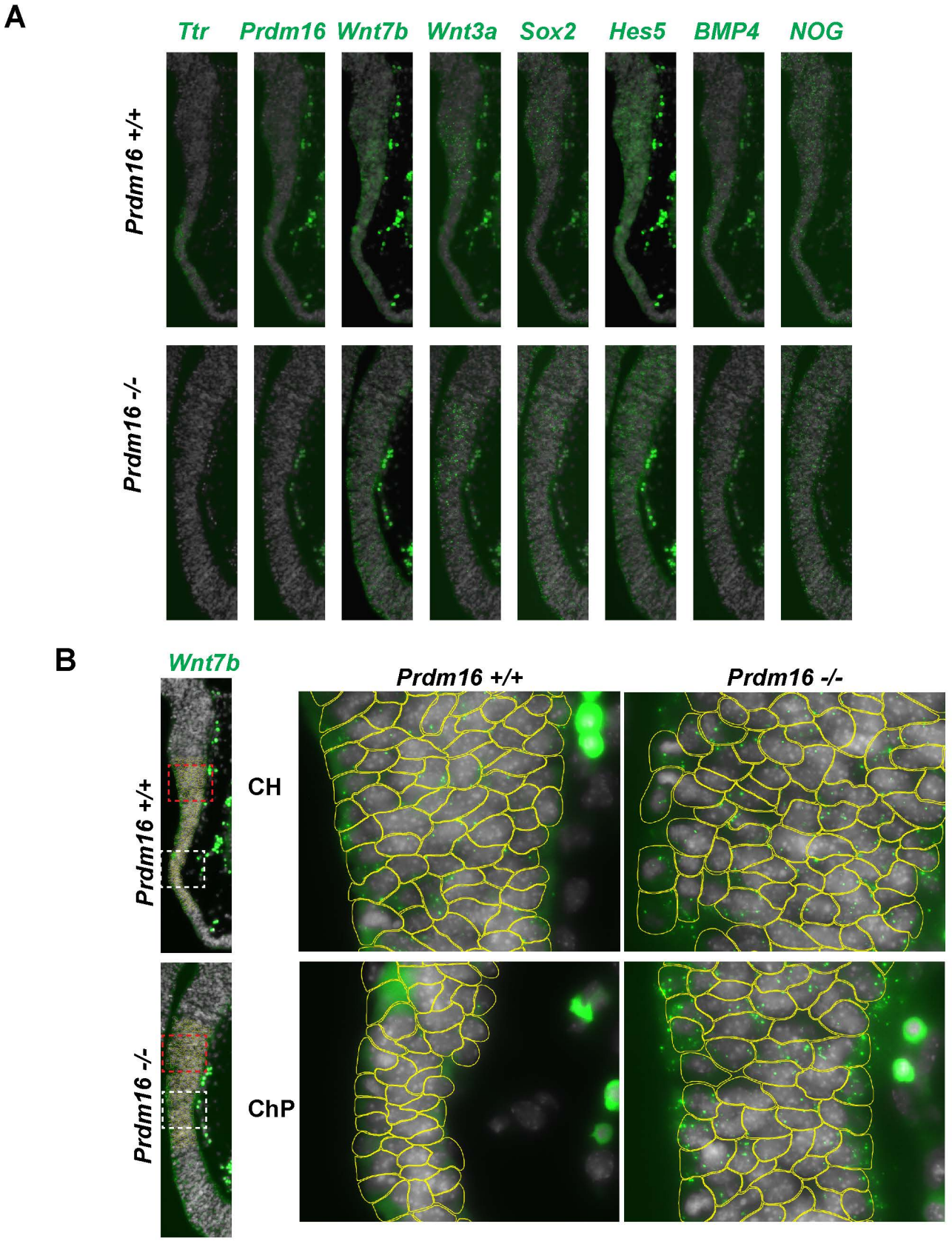
A
Ttr
Prdm16
Wnt7b
Wnt3a
Sox2
Hes5
BMP4
NOG
Prdm16 +/+
Prdm16 -/-
B
Wnt7b
Prdm16 +/+
Prdm16 -/-
CH
ChP
Prdm16 +/+
Prdm16 -/-

A

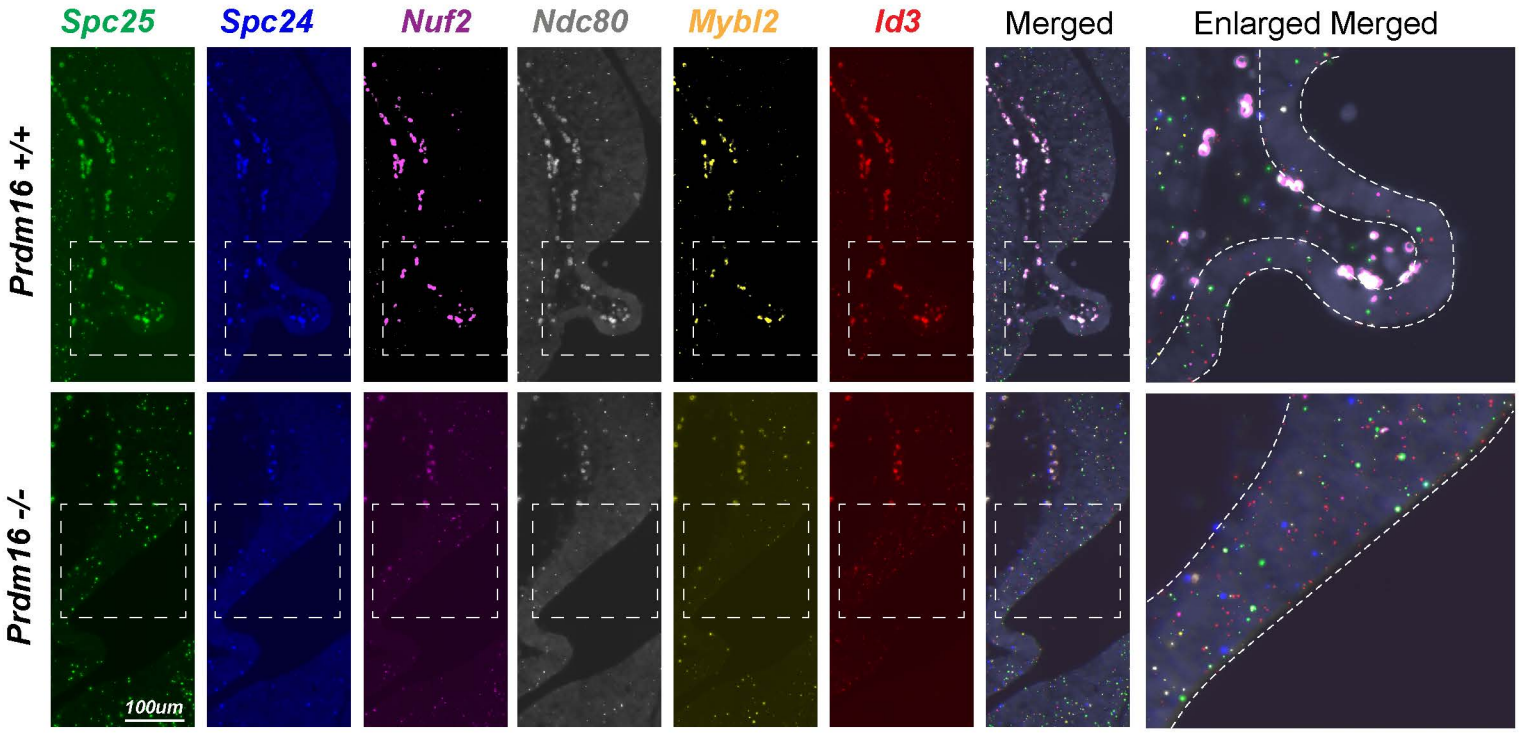
Spc25
Spc24
Nuf2
Ndc80
Mybl2
Id3
Merged
Enlarged Merged
Prdm16 +/+
Prdm16 -/-
100um

B

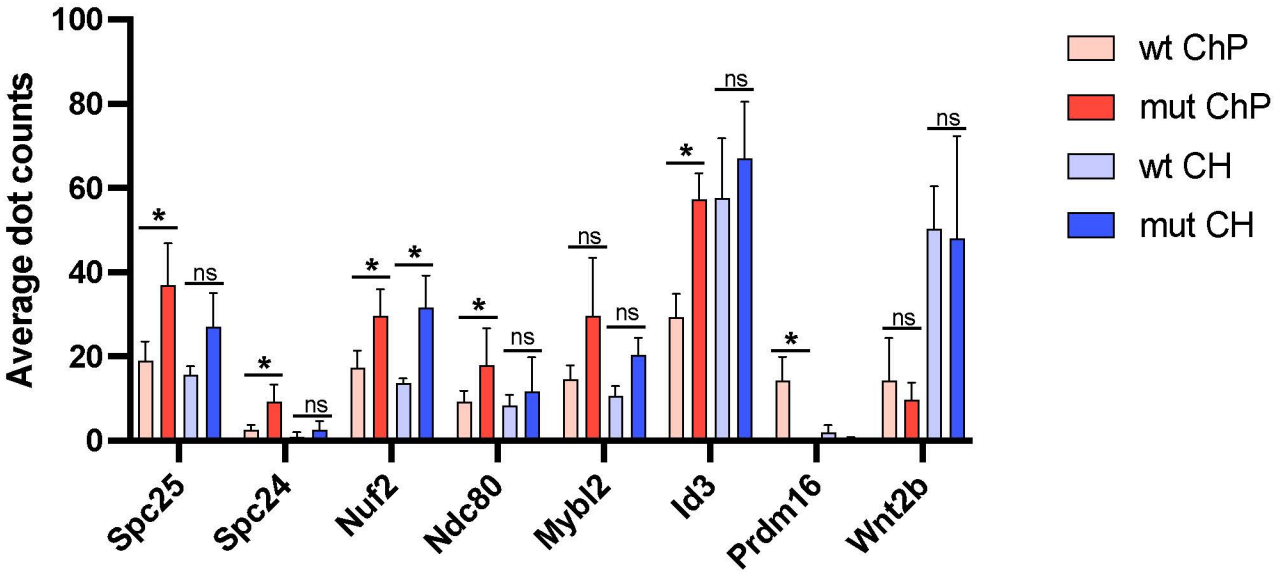
Average dot counts
100
80
60
40
20
0
Spc25
Spc24
Nuf2
Ndc80
Mybl2
Id3
Prdm16
Wnt2b
*
ns
wt ChP
mut ChP
wt CH
mut CH